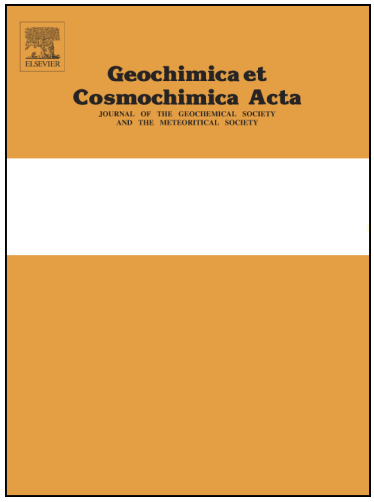

Across-arc geochemical variations in the Southern Volcanic Zone, Chile (34.5-38.0°S): Constraints on Mantle Wedge and Slab Input Compositions

G. Jacques, K. Hoernle, J. Gill, F. Hauff, H. Wehrmann, D. Garbe-Schönberg, P. van den Bogaard, I. Bindeman, L.E. Lara

PII: S0016-7037(13)00289-5
DOI: http://dx.doi.org/10.1016/j.gca.2013.05.016
Reference: GCA 8273

To appear in: *Geochimica et Cosmochimica Acta*

Received Date: 7 September 2012
Accepted Date: 13 May 2013

Please cite this article as: Jacques, G., Hoernle, K., Gill, J., Hauff, F., Wehrmann, H., Garbe-Schönberg, D., van den Bogaard, P., Bindeman, I., Lara, L.E., Across-arc geochemical variations in the Southern Volcanic Zone, Chile (34.5- 38.0°S): Constraints on Mantle Wedge and Slab Input Compositions, *Geochimica et Cosmochimica Acta* (2013), doi: http://dx.doi.org/10.1016/j.gca.2013.05.016

Across-arc geochemical variations in the Southern Volcanic Zone, Chile (34.5- 38.0°S): Constraints on Mantle Wedge and Slab Input Compositions

G. Jacques[1]*, K. Hoernle[1,2], J. Gill[3], F. Hauff[2], H. Wehrmann[1], D. Garbe-Schönberg[4], P. van den Bogaard[1,2], I. Bindeman[5], L.E. Lara[6]

[1]Collaborative Research Center (SFB574), University of Kiel and GEOMAR, 24148 Kiel, Germany

[2]GEOMAR Helmholtz Centre for Ocean Research Kiel, 24148 Kiel, Germany

[3]University of California, Santa Cruz CA 95064, USA

[4]Institute of Geosciences of the University of Kiel, 24118 Kiel, Germany

[5]University of Oregon, Eugene OR 97403, USA

[6]Servicio Nacional de Geología y Minería, Santiago, Chile

*Corresponding author:
Guillaume JACQUES
GEOMAR Helmholtz Center for Ocean Research Kiel
Wischhofstraße 1-3
24148 Kiel Germany
gjacques@geomar.de

Abstract:

Crustal assimilation (e.g. Hildreth and Moorbath, 1988) and/or subduction erosion (e.g. Stern, 1991; Kay et al., 2005) are believed to control the geochemical variations along the northern portion of the Chilean Southern Volcanic Zone. In order to evaluate these hypotheses, we present a comprehensive geochemical data set (major and trace elements and O-Sr-Nd-Hf-Pb isotopes) from Holocene primarily olivine-bearing volcanic rocks across the arc between 34.5-38.0°S, including volcanic front centers from Tinguiririca to Callaqui, the rear arc centers of Infernillo Volcanic Field, Laguna del Maule and Copahue, and extending 300 km into the backarc. We also present an equivalent data set for Chile Trench sediments outboard of this profile. The volcanic arc (including volcanic front and rear arc) samples primarily range from basalt to andesite/trachyandesite, whereas the backarc rocks are low-silica alkali basalts and trachybasalts. All samples show some characteristic subduction zone trace element enrichments and depletions, but the backarc samples show the least. Backarc basalts have higher Ce/Pb, Nb/U, Nb/Zr, and Ta/Hf, and lower Ba/Nb and Ba/La, consistent with less of a slab-derived component in the backarc and, consequently, lower degrees of mantle melting. The mantle-like $\delta^{18}O$ in olivine and plagioclase phenocrysts (volcanic arc = 4.9-5.6 and backarc = 5.0-5.4 per mil) and lack of correlation between $\delta^{18}O$ and indices of differentiation and other isotope ratios, argue against significant crustal assimilation. Volcanic arc and backarc samples almost completely overlap in Sr and Nd isotopic composition. High precision (double-spike) Pb isotope ratios are tightly correlated, precluding significant assimilation of older sialic crust but indicating mixing between a South Atlantic Mid Ocean-Ridge Basalt (MORB) source and a slab component derived from subducted sediments and altered oceanic crust. Hf-Nd isotope ratios define separate linear arrays for the volcanic arc and backarc, neither of which trend toward subducting sediment, possibly reflecting a primarily asthenospheric mantle array for the volcanic arc and involvement of enriched Proterozoic lithospheric mantle in the backarc. We propose a quantitative mixing model between a mixed-source, slab-derived melt and a heterogeneous mantle beneath the volcanic arc. The model is consistent with local geodynamic parameters, assuming water-saturated conditions within the slab.

1. Introduction:

The Chilean Southern Volcanic Zone (SVZ) extends from 33°S, just south of where the Juan Fernandez ridge is subducting and the crust of the overriding plate is ~60 km thick, to 46°S where the Chile Ridge is subducting and the crust is ~30 km thick. About 70% of the Chilean population live close to some of the most active volcanoes in the Andes along the SVZ (Stern, 2004). In this paper we report data for an across-arc profile between 34.5-38.0°S that overlaps and extends slightly further south than the Transitional Southern Volcanic Zone (TSVZ), 34.5-37.0°S, of Tormey et al. (1991). We also report data for trench sediments being subducted outboard of this region. The 1932 eruption at Quizapu volcano, one of the largest Plinian eruptions of an Andean volcano in historical time and older highly explosive silicic ignimbrite-forming eruptions that formed giant calderas, such as the Diamante caldera, took place in this part of the SVZ.

There are several potential sources for arc magmas in continental margin subduction zones: the subducting slab (including pelagic and continentally-derived trench sediments, seawater-altered upper oceanic crust, lower oceanic crust and possibly serpentinites in the subducting lithospheric mantle), the overlying mantle wedge, and the overriding lithosphere (including both continental crust and lithospheric mantle). In order to evaluate the relative role of these potential sources in generating the volcanism in the TSVZ, we present a new and comprehensive geochemical data set, including major and trace elements and Sr, Nd, Hf, O and high resolution Pb double spike isotope ratios, for primarily olivine-bearing Holocene and Late Pleistocene lavas and trench sediments from the region. Our igneous samples are from both the volcanic arc (VA), which includes the volcanic front in Chile and the rear arc up to 70 km behind the volcanic front in Chile/Argentina, and backarc (BA) volcanic centers in Argentina that are 100 to 300 km behind the volcanic front.

2. Geological setting:

Andean volcanism results from the subduction of the Nazca (7-9 cm/year towards the northeast) and Antarctic plates (2 cm/year) beneath the South American Plate (Norabuena et al., 1998; Angermann et al., 1999). The Andean cordillera is more than 7,500 km long, extending

from Colombia to southern Chile. There are four active segments divided by volcanic gaps. They have been termed the Northern Volcanic Zone (NVZ; 5°N-2°S) in Colombia and Ecuador, the Central Volcanic Zone (CVZ; 14-27°S) in Peru and northern Chile, the Southern Volcanic Zone (SVZ, 33-46°S) in central Chile, and the Austral Volcanic Zone (AVZ; 49-55°S) in southern Chile. Volcanism occurs when the slab dip angle is steep (>25°), whereas volcanic gaps occur where subduction dip angles are shallow (<10°) (Stern, 2004).

The SVZ consists of over 60 Quaternary volcanoes in Chile and Argentina, three silicic caldera systems and numerous minor eruptive centers (Stern, 2004). The SVZ has been divided into the Northern Southern Volcanic Zone (NSVZ; 33°-34.5°S; e.g. Hildreth and Moorbath, 1988), the Transitional Southern Volcanic Zone (TSVZ; 34.5-37°S; e.g. Tormey et al., 1991), the Central Southern Volcanic Zone (CSVZ; 37.0-41.5°S; e.g. Hickey-Vargas et al., 1984, 1986, 1989) and the Southern Southern Volcanic Zone (SSVZ; 41.5-46°S; e.g. Naranjo and Stern, 2004), based on the geochemical characteristics of the erupted rocks (see also López-Escobar et al., 1995) (Figure 1a). Other authors have divided the SVZ differently (e.g. Dungan et al., 2001): the Tupungato-Maipo Segment (TMS, 33°-34.2°S), located entirely on thick crust; the Palomo-Tatara Segment (PTS, 34.7°-36°S), where the frontal arc centers lie west of the continental divide; and the Longaví-Osorno Segment (LOS, 36.2°-42°S), where the southernmost chain lies near the topographic front of the Cordillera (see also Sellés et al., 2004 for further discussion of SVZ segmentation).

The TSVZ and related backarc centers, which provide information on the mantle wedge composition, are the focus of this study (Figure 1b). Our volcanic arc (VA) samples are from nine Quaternary centers at the volcanic front that are denoted by blue circles in Figure 1b for centers north of 36°S (Tinguiririca, Planchón-Peteroa, and the Los Hornitos and the Resolana cones in the area of Cerro Azul), referred to as the northern volcanic arc, and blue diamonds for centers south of 36°S (San Pedro and its nearby cones, Nevado del Longaví, Chillán and its nearby cones, Antuco and Callaqui), referred to as the southern volcanic arc. It also includes three areas in the rear arc, located up to 70 km behind the front. From north to south they are the Infernillo Volcanic Field (Folguera et al., 2009, Gudnason et al., 2012), the Laguna del Maule volcanic complex (Hildreth et al., 2010), and the Copahue stratovolcano. They are grouped together as rear arc volcanism in the tables but included in the appropriate VA group in the figures.

The backarc (BA) domain, from 100 km to 300 km behind the volcanic front is known as the Payenia volcanic field (Munoz and Stern, 1988, Stern, 1989) and volcanic centers are denoted by open symbols in Figure 1b. Some authors include the Payenia field in the larger Patagonian mafic volcanic province (Kay et al, 2004, Bertotto et al., 2009), while others keep it separate for geological and tectonic reasons (Ramos and Folguera, 2011). The Payenia volcanic field covers more than 40,000 km^2 between 34°S-38°S with an estimated volume of 8400 km^3 erupted from more than 800 centers in the last 2 Ma. The K-Ar ages of the volcanic centers between 34.5° and 35.5° range from 1.8 to <0.01 Ma (Folguera et al., 2009; Ramos and Folguera, 2011 and references therein). Eruptions were episodic with distinct spatial and temporal patterns. Eruptions near San Rafael in the north took place between 1.8-0.7 Ma, whereas those near Malargüe were younger, 0.1-0.01 Ma. The Pampas Negras volcanic field erupted from 320 ka to recent, and the Auca Mahuida field (including Auca Mahuida Volcano and cinder cones to the north along the Rio Colorado) erupted between 2.1-0.34 Ma (Gudnason et al., 2012). We have divided the Payenia volcanic field into three segments: northern, central and southern. Our samples from the northern BA segment (NBA between 34.5-35.5°S; open circles in the figures), behind the northern volcanic front, are from the monogenetic cones near San Rafael and Malargüe, and the Cerro Diamante stratovolcano and nearby cones. Samples from the Cerro Diamante stratovolcano are denoted with a circle enclosing a cross, because it may be affected by processes related to the Miocene volcanic front (Kay et al., 2004, 2005, 2006abc and references therein). The central segment samples are from the Late Pleistocene to Holocene Pampas Negras cones (36.0-36.5°S; open triangles in the figures) at the western end of a rift system extending from the Payún Matrú caldera. The southern BA segment (SBA between 37.0-38.0°S; open squares in the figures) includes the Auca Mahuida shield volcano that is farthest from the VA, the Rio Colorado volcanic field, and the Tromen stratovolcano (open crosses). The Buta Ranquil sample (open cross with a dot inside) is from a monogenetic cone at the foot of Tromen. The Tromen samples may have been affected by the same processes as at Cerro Diamante. Most samples are Late Pleistocene to Holocene in age (Table 1).

The subducted Nazca Plate formed at the East Pacific Rise north of the Valdivia Fracture Zone (40°S) and at the Chilean Rise further south (Herron et al., 1981; Tebbens et al., 1997 a,b). Its age increases towards the north, from ~30 Ma at 38°S to ~35 Ma at 34.5°S. Only one fracture zone appears to be subducting beneath the TSVZ - an extension of the Mocha Fracture Zone at

38°S that might project beneath the area near Longaví (Sellés et al., 2004; Contreras-Reyes, 2008). This fracture zone, however, is not nearly as prominent as the Valdivia and other fracture zones further south (Figure 1a).

The trench contains up to 2.2 km of sediments (Contreras-Reyes et al., 2008). Chilean trench sediments are mostly continentally-derived turbidites eroded from the Andean arc (Völker et al., 2008). Their trace element and Sr-Nd-Pb isotope compositions are similar to those of the Cretaceous to Holocene magmatic arc (Lucassen et al., 2010). ODP site 1232 is located at 39.9°S, 75.9°W in the Chile basin on the Nazca Plate ~50 km outboard of the trench (Figure 1b). Its sediments are mostly continentally-derived turbidites (Mix et al., 2003; Lucassen et al., 2010).

The crust beneath the VA, especially from San Pedro to Tinguirririca where the volcanic front steps eastward onto the Cordillera, is believed to be relatively thick based on interpretations of regional gravity data (~35-45 km, Hildreth and Moorbath, 1988; Völker et al., 2011), but thinner than in the NSVZ where it reaches a maximum thickness of 60 km. The exposed basement of the volcanic arc consists primarily of Mesozoic and Cenozoic volcanic and sedimentary rocks intruded by Miocene to Pliocene plutons. Near the coast, metamorphic meta-sedimentary rocks are intruded by Carboniferous to Permian batholiths (e.g. Stern, 2004; Lucassen et al., 2004; Cembrano and Lara, 2009). In the backarc, the San Rafael block consists of Paleozoic rocks that were uplifted during the late Miocene. There is evidence of extensional deformation in the areas where crustal attenuation occurred (Gilbert et al., 2006, Yuan et al., 2006). The depth of the slab beneath the TSVZ volcanic front is relatively uniform in this part of Chile and lies between 120 and 140 km (Tassara et al., 2006). Due to relatively uniform crustal thicknesses and depths to the slab, the thickness of the intervening asthenospheric wedge beneath the VA is also relatively uniform and ranges from 60 to 80 km (Tassara et al., 2006; Völker et al., 2011). Magnetotelluric data indicate the presence of a low resistivity plume-like zone beneath the Payenia volcanic field, presently concentrated under the Payún Matrú caldera. This region of low resistivity is rooted deeper than 200 km, just above the projected Nazca Plate (Burd et al., 2008, Ramos and Folguera, 2011).

3. Sample collection, preparation, and analytical methods:

The youngest and freshest, mostly olivine-bearing volcanic rocks (lava and tephra) were collected from each volcanic area along the volcanic front from Tinguiririca to Callaqui volcanoes and in the adjacent BA from 34.5°S to 38°S. During fieldwork, units containing xenolithic or xenocrystic material were avoided or only sampled where there was no obvious foreign material present, in an attempt to minimize crustal contamination. Their GPS-based locations, the presence or absence of olivine phenocrysts, and age estimates are presented in Table 1. We also collected sediment samples during the October 2010 RV SONNE SO210 cruise. They come from gravity cores taken from the incoming Nazca Plate (12 m length) and from the Biobio Canyon in the trench (6 m length) (33.20°-36.63°S, Figure 1b). Descriptions of the cores are available in the SO210 cruise report (Linke et al., 2011, www.dfg-ozean.de/fileadmin/DFG/Berichte_METEOR/Fahrtbericht__Sonne_210.pdf). The cores were relatively homogeneous, consisting mostly of clay, silt, and sand derived mostly from the volcanic arc (Lucassen et al., 2010). We avoided ash layers in order to minimize the direct input of arc products. Two representative samples per core were analyzed.

Hardrock samples were crushed, sieved, and washed in distilled water in an ultrasonic bath. In order to minimize the effects of alteration and crustal contamination, 5-10 g of 1-2 mm size chips were carefully handpicked under a binocular microscope to ensure selection of the freshest part of the rock and to avoid xenocrystic and xenolithic material and tephra or lava pieces with vesicle fill. Handpicked chips were powdered in an agate mill to obtain homogenous powders for XRF and ICPMS analysis. Chips were used for isotope analysis. Fresh olivine and plagioclase phenocrysts were carefully selected for oxygen isotope analysis to avoid inclusions and attached matrix.

Major element compositions were obtained at GEOMAR and at the Institute of Geosciences at the University of Kiel, both on a Phillips X'Unique PW 1480 XRF. Several reference materials (JB-2, JB-3, JA-2, BHVO-2, HTB-1, OU) were also analyzed, and yielded deviations of <5% from the published reference values (Govindaraju, 1994; Potts and Kane, 2005; Webb et al., 2009). The sediments were analysed at the University of Hamburg on a MagixPro PW 2540 XRF.

Matrix glass compositions of Planchón-Peteroa, Los Hornitos and Antuco samples were determined by electron microprobe with a Jeol JXA 8200 at GEOMAR, using polished glass shard mounts and petrographic thin sections. An accelerating voltage of 15 kV and current

of 10 mA was applied; the beam was set to 10 μm in diameter with a count time of 20 seconds per major element. Na was analyzed first to minimize element loss. The instrument was calibrated and monitored using natural reference materials VG-2 (USNM 111240/52), VGA-99 (USNM113498), ALV-981 (R23-5), and CFA-47. The reported composition is an average of 20-50 measurements.

Thirty-seven trace elements (Li, Sc, V, Cr, Co, Ni, Cu, Zn, Ga, Rb, Sr, Y, Zr, Nb, Sn, Cs, Ba, rare earth elements (REE), Hf, Ta, Pb, Th, U) were determined by ICP-MS using an Agilent 7500cs at the University of Kiel. Analytical procedures are described by Garbe-Schönberg (1993). The sediments were digested using PARR bombs in an oven in order to maximize zircon dissolution. Accuracy of analytical results was assessed with rock reference materials BHVO-2 and JA-2 analyzed as unknowns (Table 1). Average accuracy of the results (in % deviation from GeoReM's recommended values)) was better than 4% for all elements except Sc, Cr and Th in BHVO-2, and Cr, Zr, Nb and Hf in JA-2, being better than 10% for these elements. The average instrumental precision of the measurements as estimated from multiple analyses distributed over 5 to 6 hours is typically better than 1% for almost all elements. The average reproducibility of the digest procedure was monitored by duplicate preparation of at least every tenth sample and found to be better than 1%.

Sr, Nd and Pb isotope ratios were determined on ThermoFinnigan TRITON (Sr, Nd) and Finnigan MAT 262-RPQ2+ (Pb) thermal ionization mass spectrometers at GEOMAR. Pb analyses were carried out using a double spike method. A detailed description of the chemical and TIMS analytical procedures can be found in Hoernle et al. (2008, 2011). 100-150 mg of 0.5-2 mm sized, fresh rock chips were first leached in 2N HCl at 70°C for 1-2 hours and then triple-rinsed with ELGA water to remove possible surface contamination. Sr and Nd isotope ratios were mass-bias corrected within run to $^{86}Sr/^{88}Sr = 0.1194$ and $^{146}Nd/^{144}Nd = 0.7219$ and all errors are reported at the 2σ confidence level. NBS987 and our in-house Nd SPEX reference material were measured every 4th to 5th sample to obtain a normalization value for each turret relative to our preferred values of $^{87}Sr/^{86}Sr = 0.710250$ for NBS987 and $^{143}Nd/^{144}Nd = 0.511715$ for SPEX (corresponding to $^{143}Nd/^{144}Nd = 0.511850$ for La Jolla, Krolikowska-Ciaglo et al., 2005). The normalization value was then applied to the sample data for each turret. This procedure compensates for machine drift over the course of the project (2009-2012) and therefore allows maximum data comparability. External 2σ uncertainties are ± 0.000011 (n= 25) for NBS987 and

± 0.000005 for SPEX. Long term machine drift for $^{143}Nd/^{144}Nd$ and $^{87}Sr/^{86}Sr$ between 2008 and 2012 is within 0.000030. The double spike corrected NBS981 values measured along with the samples are $^{206}Pb/^{204}Pb$ = 16.9413 ± 21, $^{207}Pb/^{204}Pb$ = 15.4994 ± 20, $^{208}Pb/^{204}Pb$ = 36.7241 ± 56, $^{207}Pb/^{206}Pb$ = 0.914889 ± 37, $^{208}Pb/^{206}Pb$ = 2.16773 ± 13 (n=38), and compare well with published double and triple spike data for NBS981 (see Hoernle et al., 2011). Total Pb chemistry blanks were determined for each sample batch and were below 25 pg, with the exception of a single Pb blank of 200 pg. Sr-Nd chemistry blanks are typically below 100 pg and 50 pg, respectively. These blank levels are negligible even relative to the amount loaded on the filaments (60-80 ng Pb and 500-1000 ng Sr and Nd). Replicate analyses by means of separate digestions are within the external 2σ reproducibility of the Sr-Nd-Pb reference materials stated above.

Hf isotopes were determined on a NU Plasma HR MC-ICPMS at GEOMAR. 200-500 mg of 0.5-2 mm sized fresh rock chips were digested for 60 hours at 130°C in a HF-HNO_3 mixture. Details of the chemical separation procedures are reported in Blichert-Toft et al. (1997) and Geldmacher et al. (2006). Prior to analysis, samples were diluted to 80-100 ppb Hf to obtain a total Hf beam of 12-14 V. Hf isotope ratios were measured using static multi-collection and were mass-bias corrected to $^{179}Hf/^{177}Hf$ = 0.7325 assuming exponential mass fractionation. Our in-house Hf reference material solution SPEX was measured every 3 to 5 samples to obtain a normalization value for each sample sequence. Over the course of the project (2010-2012), our in-house SPEX reference material solution had $^{176}Hf/^{177}Hf$ = 0.282170 ± 6 (2σ, n = 45), which corresponds to $^{176}Hf/^{177}Hf$ = 0.282163 for JMC-475 (Blichert-Toft et al., 1997).

Oxygen isotope analyses were performed at the University of Oregon using CO_2-laser fluorination (e.g. Bindeman, 2008) and a Newwave 35W CO_2 laser. Single and bulk phenocryst grains, ranging in weight from 0.6-2 mg, were reacted in the presence of BrF_5 to liberate oxygen gas (protocol #1 in Table 2). The gas generated in the laser chamber was purified through a series of cryogenic traps held at liquid nitrogen temperature, and a mercury diffusion pump was used to remove traces of fluorine gas. Oxygen was converted to CO_2 gas in a small platinum graphite converter, the yield was measured, and then CO_2 gas was analyzed on a MAT 253 mass spectrometer. Four to seven aliquots of internal garnet reference material (UOG1, $\delta^{18}O$ = 6.56‰, calibrated against the Gore Mt. Garnet ($\delta^{18}O_{olivine}$ = 5.8‰ VSMOW, Valley et al., 1995)), as well as aliquots of reference materials (mantle olivine from San Carlos with $\delta^{18}O_{olivine}$ = 5.25‰,

Bindeman, 2008) were analyzed together with the unknowns during each analytical session. Between-run variability of the measured $\delta^{18}O_{olivine}$ values of the reference materials ranged from 0.1 to 0.25‰ less than their accepted value, and samples values were adjusted to correct for this small day-to-day variability. The average precision of reference materials and duplicates of single grains and bulk analyses was in the range ±0.02 to ±0.08‰ (1σ).

For oxygen isotope analysis of bulk sediment, powdered sediments were heated at 150°C in a vacuum oven overnight to remove any loosely absorbed environmental water. Then one of two protocols was used: 1) minimal BrF_5 pretreatment of multiple samples hard-pressed into holes in a holder in a laser fluorination chamber (protocol #2 in Table 2); or 2) one-by-one analysis in a regular chamber or an air-lock sample chamber (protocol #3). As demonstrated with other clay-rich sediments, there is systematic ~1‰ difference between these two methods because of rapid BrF_5 stripping of loosely-bound H_2O in clays. Although it remains unclear which protocol is more appropriate for subducted sediment, we favor results from protocol #2.

4. Results:

Sixty volcanic samples were analyzed for major elements, trace elements and Sr, Nd and Pb isotope compositions, twenty-three for Hf isotopes, and nineteen for O isotopes. Ten sediment samples were analyzed for major and trace elements, five for Sr-Nd-Pb isotopes, four for Hf isotopes, and seven for O isotopes. The data are presented in Table 1 (major and trace elements) and in Table 2 (Sr-Nd-Hf-Pb-O isotopes).

VA samples consist primarily of basalts to andesites/trachyandesites with SiO_2 = 51-61 wt. % and MgO = 2.8-8.5 wt. %, with the exception of one sample that plots on the andesite/dacite boundary (Figure 2). About half of our VA samples have MgO > 5% and SiO_2 < 54%. They are mostly calc-alkalic (they lack Fe-enrichment). Three from Tinguiririca, one from San Pedro and one from Copahue plot in the high-K field of Gill (1981) (not shown). In MgO versus major element oxide diagrams (Figure 3), the VA samples have positive correlations of MgO versus FeOt (total iron as FeO) and CaO (Figure 3a,b), and negative correlations of MgO versus Al_2O_3, Na_2O (Figure 3c,d), SiO_2, and K_2O (not shown).

BA samples are more mafic alkali basalts and trachybasalts with SiO_2 = 45-50 wt. % and MgO = 4-11 wt. %, except for three trachyandesite (Figures 2 and 3). Most Pampas Negras

samples are evolved with MgO = 4-6 wt. %. BA samples have similar correlations between MgO and the other oxides as observed for the VA samples. Relative to the VA, the BA trend is shifted to lower SiO_2 (Figure 2) but higher FeOt, Na_2O, TiO_2, P_2O_5 (Figure 3a,d,e,f), K_2O and MnO contents (not shown) and lower concentrations of most incompatible trace elements (e.g. Zr, Hf, Nb, Ta, REE and Ba). There is little or no overlap between VA (including rear arc) and BA samples for Ti, Na, and P, and the change occurs between 70 and 100 km behind the volcanic front.

All VA samples show typical subduction zone incompatible element signatures, characterized by enrichment in fluid-mobile Large Ion Lithophile Elements (LILE), such as Cs, Rb, Ba, U, K and Pb, and depletion in the High Field Strength Elements (HFSE) Nb and Ta, relative to light REE (Figure 4a). Differentiated VA samples show relative enrichment in Zr and Hf, and depletion in Ti. BA samples have similar patterns but overall greater enrichment in highly incompatible elements, steeper heavy REE patterns (Sm/Yb in VA = 1.48-2.25, in BA = 2.26-4.32), and less pronounced negative Nb and Ta troughs (Figure 4b). Consequently, the VA samples have higher fluid-mobile (e.g. LILE) to fluid-immobile (e.g. HFSE and REE) element ratios (e.g. higher Ba/La, Ba/Nb and Th/Nb and lower Ce/Pb, Nd/Pb, Nb/U), and lower ratios of more to less incompatible HFSE and REE ratios (e.g. lower Nb/Zr, Nb/Y, Ta/Hf, Zr/Hf, Nb/Yb, Ta/Yb, Gd/Yb, Tb/Yb, TiO_2/Yb) than the BA samples. In general, some NBA and Tromen samples show a more pronounced subduction zone signature than other BA groups. Sample CL 472 from Buta Ranquil near Tromen shows the most pronounced subduction zone signature in the BA.

Our $^{87}Sr/^{86}Sr$ and $^{143}Nd/^{144}Nd$ isotope data are similar to those of previous studies for the TSVZ (Hildreth and Moorbath, 1988; Tormey et al., 1995; Davidson et al., 1987, 1988; Hickey-Vargas et al., 1986; Harmon et al., 1984; Sigmarsson et al., 1990) and the BA (Kay et al., 2006a,b,c; Varekamp et al., 2010). $^{87}Sr/^{86}Sr$ vs. $^{143}Nd/^{144}Nd$ isotopes are negatively correlated for both VA and BA samples, the VA and BA data almost completely overlap, and both lie within the South Atlantic Mid-Ocean Ridge Basalt (MORB) field (Figure 5). The Buta Ranquil sample is displaced to higher Nd and/or Sr isotope ratios and has the highest Nd isotope ratio of the samples we analyzed, while the other Tromen samples plot together with the other BA samples. The trench sediments largely overlap the volcanic rocks in Nd, but extend to higher Sr isotope

ratios. Most of the sediments that we analysed lie at the enriched end of the Chilean trench sediment field in Figure 5 defined by data from Lucassen et al. (2010).

The Pb isotope data for VA and BA samples have the same tight positive correlations on uranogenic Pb (r^2 = 0.92 or 0.94 excluding the Buta Ranquil sample) and thorogenic Pb (r^2 = 0.96 or 0.97) isotope diagrams (Figures 6a,b). This is a much tighter array than for older unspiked data (e.g. Hildreth and Moorbath, 1988; Tormey et al., 1995; Davidson et al., 1987, 1988, not shown). The VA samples (with $^{206}Pb/^{204}Pb$ = 18.56-18.65) fall almost completely within the field for the Chilean trench sediments and cover nearly the full range in $^{206}Pb/^{204}Pb$ ratios of the sediments, whereas the backarc samples (with $^{206}Pb/^{204}Pb$ = 18.30-18.61) extend to significantly less radiogenic ratios. The southern and central part of the BA have the least radiogenic Pb isotopic compositions, whereas the NBA, Tromen and Buta Ranquil have Pb isotope ratios intermediate between the VA and the southern BA and are shifted to slightly lower $^{207}Pb/^{204}Pb$ at a given $^{206}Pb/^{204}Pb$ isotope ratio (towards a Pacific MORB component). Pb isotope ratios (e.g. $^{206}Pb/^{204}Pb$) correlate well with Nb/Zr (r^2 = 0.70), Nb/U (r^2 = 0.84), Ce/Pb (r^2 = 0.81) (Figure 7), if the BA samples from Buta Ranquil and the Cerro Diamante stratovolcano are excluded. The correlations within individual volcanic centers are slightly more scattered, especially for the VA samples which overlap the Chilean trench sediment field on these diagrams.

The samples form two subparallel positive arrays on a plot of Nd versus Hf isotope ratios with the VA samples (r^2 = 0.87) having higher εHf for a given εNd than the BA samples (r^2 = 0.79) (Figure 8). We know of no other arc like this (cf. Pearce et al., 1999, Woodhead et al., 2001, 2012, Tollstrup and Gill 2005, Yodozinski et al., 2010). The Chilean trench sediment outboard of the TSVZ is displaced above the VA field, which we attribute to the presence of a pelagic component, while sediments from the Peru/Chile trench >2000 km farther north have lower εNd than any of the TSVZ volcanic rocks (Vervoort et al., 1999, 2011). The most radiogenic Peru trench sediment with εHf = +4-5 slightly overlaps the least radiogenic TSVZ VA samples in εHf. The sediment from the canyon on the continental slope has similar Hf-Nd isotopes to the VA.

Oxygen isotope analyses of olivine (and two plagioclase samples normalized to olivine) define narrow ranges for both the VA (4.88 to 5.62‰ or 5.52‰ if the plagioclase value from CL 726, the most evolved sample measured for oxygen isotopes, is excluded) and BA (5.02-5.42‰)

(Figure 6c). The VA samples spread around canonical mantle olivine values (5.0-5.4‰; Mattey et al., 1994) and extend to both slightly lighter and heavier compositions. Excluding CL726, $\delta^{18}O$ for the other samples show no correlation with parameters of differentiation, such as SiO_2 (Figure 9a) or MgO content (not shown), or with incompatible elements or Sr, Nd, or Pb isotope ratios (e.g. Figure 6c).

The compositions of the SO210 trench sediments (major and trace elements and Sr-Nd-Pb isotopes) are comparable to those reported previously (Lucassen et al., 2010) and summarized by Plank (2011), except that our samples have higher Ba concentrations. Since our results for reference materials are close to expected values and the Ba data are reproducible, we exclude an analytical problem with our data. Our trench sediments are quite uniform in isotopic composition apart from the one from a canyon on the continental slope where the sediments are similar to Quaternary volcanic rocks and are likely to reflect eroded volcanic arc rocks. Our "typical" trench sediment composition in Table 3 is similar to that of Plank (2011) for 35°S and 40°S except for Ba. In order to use actual samples for representative values, we used our sample SO210-#5-B for trace elements and sample 75KD(2) from Lucassen et al. (2010) for isotopes. Sample 75KD(2) comes from a bit further south of the studied area but is similar to our sediment data (Table 1 and Table 2) and is the single best mixing end member to explain TSVZ VA volcanic rocks. Isotopically, our new sediment data and sample 75KD(2) enclose the values chosen by Plank (2011), although her values are more radiogenic than most of our samples. In general, the trench sediments and volcanic rocks are similar in composition, which is not unexpected because the trench sediments at 35°-40°S are dominated by turbidites from the Cenozoic magmatic arc delivered through canyons in the continental slope and also contain ash from the volcanic arc. The chief isotopic differences are that the sediments have considerably higher $\delta^{18}O$, ranging from 7.8-14.1‰, and higher $^{87}Sr/^{86}Sr$ relative to $^{143}Nd/^{144}Nd$.

5. Discussion:

Based on the major element data, two distinct magmatic series can be recognized in the TSVZ. The VA is subalkaline (calc-alkaline/medium-Fe) whereas the BA is alkaline with higher Ti, Na, and P (Figures 2 and 3). Compared to the BA samples, the VA samples have higher fluid mobile (LILE) and lower fluid immobile element (HFSE and heavy REE) contents, and lower

ratios of more to less incompatible HFSE and REE (e.g. Nb/Zr, Nb/Y, Nb/Yb, Ta/Yb, Gd/Yb, Tb/Yb) (e.g. Figure 7c, not all ratios shown). Due to differences in bulk distribution coefficients, these ratios can be fractionated by differing degrees of mantle melting (e.g. Green et al., 2000). In contrast, some elements that cannot be easily fractionated by mantle melting can instead be fractionated by fluids or hydrous melts from the subducted slab. Ratios of fluid-mobile (e.g. LILE) to fluid-immobile (e.g. HFSE and REE) elements (e.g. Ba/Nb, U/Nb, Pb/Ce and Pb/Nd ratios) (e.g. Figure 7a,b, not all ratios shown) are higher in VA lavas. The variations in these ratios are consistent with a higher fluid flux beneath the VA than the BA, resulting in higher degrees of melting beneath the VA (e.g., Marianas arc, Elliot et al., 1997; Kelley et al., 2006) to produce the larger volume stratovolcanoes of the VA relative to the isolated fields of cinder cones in the BA, including those on older shield and stratovolcanoes. Although the VA and BA almost completely overlap in Sr, Nd and O isotopic composition, the VA samples haves more radiogenic Pb isotopic compositions which overlap the field for Chilean Trench sediments, whereas the BA samples have less radiogenic Pb, projecting into the field for South Atlantic MORB. On the Nd versus Hf isotope diagram, the VA and BA form distinct positive linear arrays with the VA samples shifted towards more radiogenic Hf at a given Nd isotopic composition.

We will next discuss possible reasons for the differences between the VA and the BA: assimilation of the continental crust, heterogeneity of the mantle wedge, and the nature of the slab-derived component.

A. Crustal assimilation

Because the TSVZ overlies 35-45 km thick crust, crustal assimilation is a distinct possibility during magma ascent. In particular, Hildreth and Moorbath (1988) and Tormey et al. (1991) noted an increase in trace element concentrations and Sr-Nd isotopic enrichment of evolved rocks erupted north versus south of 37°S, correlating with an increase in crustal thickness to the north, and interpreted this to result from greater degrees of crustal assimilation in the north where the crust is thicker. Studies of single volcanoes north of 37°S also demonstrate that crustal contamination is possible in the more evolved magmas. Tormey et al. (1995) proposed that crustal assimilation played a role in dacitic and rhyodacitic rocks at the Azufre-

Planchón-Peteroa complex at the volcanic front, as did Hildreth et al. (2010) for the Laguna del Maule area in the rear arc. Davidson et al. (1987, 1988) studied the Tatara-San Pedro-Pellado complex in detail. They suggested that although the sub-arc asthenospheric mantle was the principle source of basalts, and their LILE enrichments were largely from slab fluids, the more evolved rocks were affected by crustal assimilation during crystal fractionation. Dungan et al. (2001) and Dungan and Davidson (2004) proposed that assimilation of mafic plutonic roots occurs sometimes in San Pedro, primarily affecting the major and trace element contents of the magmas with little effect on the radiogenic isotopic composition. Therefore, it is essential to evaluate if these processes affected the geochemistry of our samples.

We analysed the most mafic of the youngest samples that we could find at each edifice, mostly with olivine phenocrysts, because most studies of the SVZ between 34.5-43°S have concluded that the olivine basalts in the SVZ were not significantly crustally contaminated (e.g. Hickey-Vargas et al., 1984, 1986, 1989, 2002; Futa and Stern, 1988; Sigmarsson et al., 1990, 2002). We also avoided xenocrystic and xenolithic material during sampling and sample preparation. Our VA samples can be divided into a mafic group with MgO > 5 wt. % and SiO_2 < 54 wt. %, and a differentiated group with lower MgO and higher SiO_2 content. The differentiated group consists of three samples from Tinguiririca, three from San Pedro, two from Longaví, two from Antuco, one from Callaqui and one from Copahue. There is no difference between the average of mafic and evolved groups in trace element ratios or in any isotope ratio (Figure 9) and the most-evolved high-K calc-alkalic Tinguiririca samples do not have the highest Sr or lowest Nd isotope ratios (Figure 5, 9b,c). Neither the VA nor BA shows systematic variations with SiO_2 or MgO (not shown). Due to the high Pb concentrations in most crustal rocks, Pb isotopes are a very sensitive indicator of crustal assimilation. The end member VA samples, with the most radiogenic Pb isotope ratios, fall below (have lower $^{207}Pb/^{204}Pb$ than) all basement rocks with similar $^{206}Pb/^{204}Pb$ on the uranogenic Pb isotope diagram (Figure 6a; basement data from Lucassen et al., 2004; 36-41°S). Since neither the VA nor BA end member falls within the fields for the crustal basement rocks, the very tight correlations in our high-precision Pb isotope ratios preclude significant crustal assimilation having affected any of these samples. Furthermore, there is no correlation between any isotope ratio and $\delta^{18}O$ (for example, Figures 6c and 13). Thus, radiogenic isotopes show no evidence of crustal assimilation of older basement rocks, even in the andesites.

Variations in O isotope values in volcanic rocks can be used to constrain the amount of assimilation of isotopically diverse components (e.g. Bindeman, 2008). However, the $\delta^{18}O_{olivine}$ in the volcanic rocks from the VA overlap the range of mantle olivine (5.0-5.4‰, Mattey et al., 2004) and extend to only slightly higher values (5.5‰ if the most evolved sample is excluded) and lower values (4.9‰) (Figure 6c), which could reflect slightly variable contributions from lower $\delta^{18}O$ subduction fluids from the lower oceanic crust, or higher $\delta^{18}O$ subduction melts from the seawater-altered upper crust (e.g. Bindeman et al., 2005; Martin et al., 2011). The BA samples (5.02-5.42‰) are within the mantle range. In both the VA or BA samples, $\delta^{18}O$ ratios do not correlate with indices of differentiation (for example SiO_2, Figure 9a) or other isotope ratios, such as $^{207}Pb/^{204}Pb$ (not shown), which are discriminatingly higher in Andean basement rocks (Lucassen et al., 2004, Figures 6). Moreover, $\delta^{18}O$ values are within the typical range for subduction zone volcanic rocks lacking other evidence for crustal assimilation (e.g. Central America: see Heydolph et al., 2012). They are also within the range for oceanic arcs where there is less potential for crustal assimilation. The Mariana arc has whole rock $\delta^{18}O$ values between 5.5‰ and 6.6‰ (Wade et al., 2005), and Tonga arc values are between 5.6‰ and 6.8‰ (Ewart et al., 1987, Vallier et al., 1991, Turner et al., 2009). We corrected our VA phenocryst $\delta^{18}O$ values to equilibrium melt following Bindeman et al. (2004) who calculate the Δ(min.-melt) based on the SiO_2 content of the whole rock. Our corrected VA phenocryst $\delta^{18}O$ values yield a similar range of 5.9-6.5‰ (excluding the most evolved sample CL 576 with $\delta^{18}O$ melt of 7.1) (Table 2). It has been proposed that whole rock $\delta^{18}O$ up to ~6.6‰ can be inherited from a slab component (Eiler et al., 2005) or metasomatized mantle containing pyroxenitic veins from earlier arc volcanism (Heydolph et al., 2012), or a preexisting subduction enrichment (Auer et al., 2009, Martin et al., 2011).

The low $\delta^{18}O$ value for CL 531 from Longaví (4.88‰) could be explained by assimilation of hydrothermally altered mafic rocks, such as in the lower crust (with $\delta^{18}O$ = 0-6‰, Bindeman et al., 2005, and references therein), as proposed by Dungan and Davidson (2004) for San Pedro. Our samples from San Pedro do not have low $\delta^{18}O_{olivine}$, however. Alternatively, the low $\delta^{18}O$ at Longaví could possibly reflect the derivation of fluids from serpentinite associated with the Mocha Fracture Zone subducting beneath Longaví.

In summary, our isotope data show no clear evidence that assimilation of old sialic crust affected our TSVZ basalt to andesite samples. Even if there was assimilation of the mafic roots

of the volcanoes in some of our more differentiated samples, it would only add potential for sampling greater Sr-Nd-Hf-Pb isotope mantle heterogeneity throughout the Cenozoic in the vicinity of the volcanoes, and would not affect our conclusion that the primary isotopic diversity comes from the mantle, not the sialic crust.

B. The mantle wedge and subcontinental lithosphere

BA basalts have less subducted component signature in their trace element abundance patterns (Figure 4b) than the VA samples and are displaced the most from sediment in their Pb isotopic compositions (Figures 6a,b). Indeed, those from the southern and central BA extend to MORB-OIB (Ocean Island Basalt) Ce/Pb, Nd/Pb, Nb/U, and Nb/Th ratios (Hofmann et al., 1986) with little if any evidence for slab-derived Pb, U or Th (Figures 7a,b and 10-11). Therefore, we propose that BA basalts in general, and the SBA and Pampas Negras basalts in particular, best represent the geochemical character of the TSVZ BA mantle source.

On the uranogenic Pb isotope diagram (Figure 6a), the BA array lies above the Pacific MORB field. An extension of the BA trend does not intersect the Pacific MORB field but does intersect the enriched part of the South Atlantic MORB field, which has elevated $^{207}Pb/^{204}Pb$ at $^{206}Pb/^{204}Pb$ between 17.6 and 18.2. Consequently, the BA mantle source has South Atlantic rather than East Pacific Rise affinity. This is in agreement with the work of Husson et al. (2012) that modelled the flow of South Atlantic mantle beneath South America. They modelled westward mantle convection beneath South America as a counterflow above the subducting Nazca plate. Therefore, this convection brings South Atlantic Ridge mantle beneath the Andes.

Many of our BA basalts, and especially those from the SBA and Pampas Negras, are enriched in HFSE with Nb/Yb > 10, like alkalic OIB (Figure 11), and plot beneath the field for South Atlantic MORB on the Hf versus Nd isotope ratio diagram (Figure 8). Therefore, the TSVZ BA mantle may contain OIB or EMORB-type components. In contrast, VA basalts have lower Nb/Yb (Figure 11) and Nb/Zr (Figure 7c) indicating that the VA mantle source is more depleted, or has experienced higher degrees of melting or both, than the BA source. Increasing source depletion closer to the VA may reflect progressive extraction of small degree melts as a result of corner flow in the mantle wedge (Hochstaedter et al., 2001). Increasing percent melting beneath the VA is consistent with a higher mass fraction of slab flux there.

The Sr and Nd isotopes of most VA and BA basalts lie within the enriched portion of the South Atlantic MORB (SAM) field (Figure 5). In detail, those from the SBA and Pampas Negras (36-38°S), which show no evidence for the addition of slab-derived Th (Figure 11) and little addition of U and Pb (Figure 7a,b), span a range of Sr and Nd isotopes that we attribute to the mantle source. These rocks form a negative array on the Sr-Nd isotope diagram and plot at the left edge of the TSVZ VA field, having less radiogenic $^{87}Sr/^{86}Sr$ at a given $^{143}Nd/^{144}Nd$ isotope ratio. Basalts from the Resolana and Los Hornitos cones near Cerro Azul and from Tinguiririca in the northern VA (34.5-36°S) overlap the range for the southern BA lavas, excluding the Buta Ranquil sample. Therefore, the TSVZ mantle is heterogeneous in Sr and Nd, and contains both depleted (SAM-D) and enriched (SAM-E) components (Figure 12a).

Although VA and BA samples overlap almost completely on the Sr-Nd isotope diagram (Figure 5), the same is not true for Pb (Figures 6a,b) or Hf isotope ratios (Figure 8). This can be seen most easily by combining Sr and Pb isotope ratios (Figure 12b), where the northern and southern VA groups, the central and southern BA groups, and perhaps even NBA samples seem to define different mixing trends between a slab component (trench sediment ± Altered Oceanic Crust (AOC)) and variable mantle components. The northern and southern VA groups could be derived through mixing of the same end members (slab component + SAM-D) with different Pb/Sr ratios in one or both of the end members, or through mixing of slab and/or mantle components with slightly different compositions. The BA groups require a spatially heterogeneous mantle source with the addition of less slab component than at the VA. The SBA and Pampas Negras mantle end members most closely approximate the SAM-D and SAM-E components respectively.

This explanation, however, does not easily apply to the variation between Hf and Nd isotopes. The VA and BA groups define subparallel and offset positive correlations between Hf and Nd isotopes (Figure 8). Within the VA, the depleted end (with highest Nd and Hf ratios) consists of the Resolana/Los Hornitos cones that have the least radiogenic Sr and most radiogenic Nd isotope ratios and are the closest to the depleted mantle component (SAM-D in Figure 12). The more enriched VA samples do not lie on a mixing line between the depleted end and trench sediment as is the case on the $^{87}Sr/^{86}Sr$ vs. $^{206}Pb/^{204}Pb$ isotope diagram (Figure 12b). Instead they define a mixing array slightly steeper than the mantle Hf-Nd array (Geldmacher et al., 2006) such as observed in South Pacific backarc basalts (Todd et al., 2011). This mixing

array is most easily explained by mantle heterogeneity. The completely offset BA Hf-Nd array is without precedent in subduction zones to our knowledge. Apart from Central America where some BA samples also plot beneath the VA array (Heydolph et al., 2012), in no other arc do VA and BA samples define separate subparallel trends. All of these BA basalts have typical mantle Hf/Nd concentration ratios. The more depleted end of the BA Hf-Nd isotope array (SBA) also extends to the lowest Sr and Pb isotope ratios. The more enriched end of the BA array (NBA) is not offset toward subducting sediment in Nd and Hf isotopes. We think that the BA Hf-Nd trend also reflects mixing between depleted and enriched mantle components. Because the BA array is without precedent in oceanic arcs and lies below the field of South Atlantic MORB, we believe that both of its mantle components may lie within South American Proterozoic subcontinental lithosphere. Similarly low Hf with respect to Nd isotopes have been observed within continental basalts and attributed to mixing between components in subcontinental lithospheric mantle elsewhere (e.g. Zhang et al., 2009).

The restricted and mantle-like range in $\delta^{18}O$ (5.0-5.4‰) of the BA rocks suggests a source within the sub-continental lithospheric mantle. Its enriched end member may be the EM1-type mantle identified by Varekamp et al. (2010) in the Loncopue graben (37.5°-39°S, Neuquén, Argentina) that they also attributed to the subcontinental lithospheric mantle. The difference in Nb/Yb ratios between BA and VA could reflect trenchward advection and depletion of asthenospheric mantle but could also reflect a contrast between VA melts primarily derived from the asthenosphere versus BA melts that are in part from subcontinental lithospheric mantle beneath the BA. The latter may exist as delaminated old heterogeneities with lower solidi that melt out as mantle advects trenchward (Hochstaedter et al., 2001).

We also note the inconsistent correlation between trace element and isotope ratio measures of mantle enrichment and depletion. Nb/Yb and Nb/Zr ratios form crude positive correlations with $^{176}Hf/^{177}Hf$ and $^{143}Nd/^{144}Nd$ in the BA basalts (not shown), opposite to what is generally observed for the mantle (e.g. Douglass, 2000, Andres et al., 2002, Kingsley, 2002, Kingsley et al., 2007). Therefore, melting effects are superimposed on source effects within the BA basalts. The SBA basalts are farthest from the VA and reflect the lowest percent melting, because the amount of slab component fluxing is least.

Kay et al. (2004, 2005, 2006abc, and references therein) proposed that magmatism in the southern Mendoza and Neuquén provinces (which overlap and extend further south than our BA

area) resulted from melting of hydrated mantle after two temporary flat subduction episodes in the late Miocene that moved the volcanic front eastward and produced large stratovolcanoes like Tromen and Cerro Diamante. The NBA and Tromen groups exhibit more arc affinities than the rest of our BA samples by: 1) having greater positive anomalies in fluid-mobile elements (Pb, K) and negative anomalies in HFSEs (Nb, Ta), 2) plotting closest to the VA in the Ce/Pb versus Nb/U diagram (Figure 10), 3) plotting above the mantle array and close to the VA on the Nb/Yb versus Th/Yb diagram (Figure 11), 4) having higher La/Ta, Ba/Ta and Th/Hf ratios than the other BA rocks which are most similar to the VA, and 5) having Pb isotope ratios most similar to the VA rocks. This could reflect residual slab components in the lithospheric mantle and/or crust beneath this part of the BA left over from when it was near the VA in the late Miocene/Early Pliocene, or more current input of slab components beneath these parts of the BA. The addition of Paleozoic crust to the mantle wedge as a result of forearc erosion in the late Miocene (Kay et al., 2005) cannot explain the more arc-like composition of the NBA because the addition of Paleozoic metamorphic or igneous crust would increase $^{207}Pb/^{204}Pb$ ratios in the NBA, yet they tend to be lower (not higher) at a given $^{206}Pb/^{204}Pb$ compared to the VA and other BA basalts (Figure 6a).

C. The slab component

In general, fluids and/or melts can be produced by dehydration and/or melting of the slab during subduction beneath the VA and BA. Possible slab sources include the sediments, AOC, and the underlying lithospheric mantle that may have been serpentinized at bend faults and/or fracture zones. In this section we will attribute features that cannot otherwise be accounted for by crustal assimilation or mantle heterogeneity to a slab-derived component, and explore the nature of that component.

(1) Sources of the slab component

The incompatible element ratios of trench sediments almost completely overlap those of VA volcanic rocks in part because the former are almost entirely derived from the latter. Nonetheless, their similarity in Figure 4a means that the currently subducting sediments may be

618 responsible for the trace element pattern of the currently erupting magmas. Pb isotopes confirm
619 this observation because most of the Pb in the volcanic rocks is from the slab component. On
620 both the uranogenic and thorogenic Pb isotope diagrams (Figures 6a,b), the TSVZ data form
621 excellent positive correlations ($r^2 = 0.94$ and $r^2 = 0.97$ respectively if the Buta Ranquil sample is
622 excluded), with the VA samples falling at the radiogenic end of the Pb isotope arrays and
623 covering most of the sediment range in $^{206}Pb/^{204}Pb$. Therefore, most of the fluid-mobile Pb must
624 come from the sediment. This is confirmed by the overlap between VA and sediment in Figure 7.
625 However, there is permissive evidence that some of the Pb also comes from the AOC slab
626 component. The most radiogenic VA samples plot at the base of or just below the sediment field,
627 suggesting that some of the Pb comes from an AOC component with lower $^{207}Pb/^{204}Pb$ and
628 $^{208}Pb/^{204}Pb$ at a given $^{206}Pb/^{204}Pb$. We cannot constrain this tightly because of uncertainty in the
629 Pb isotopic composition of all components and the circularity of argument about whether the
630 sediments control the VA magmas or vice versa. However, the subducting crust is from the East
631 Pacific Rise and should have a composition similar to Pacific MORB. Therefore more oceanic
632 crust in the slab component will decrease its $^{207}Pb/^{204}Pb$ and $^{208}Pb/^{204}Pb$ relative to $^{206}Pb/^{204}Pb$
633 ratios. This argument takes advantage of the difference in Pb isotopes between the subducting
634 altered oceanic crust (Pacific-type) versus mantle wedge (South Atlantic-type) sources. The
635 NBA samples have lower $^{207}Pb/^{204}Pb$ ratios than VA samples with similar $^{206}Pb/^{204}Pb$, suggesting
636 a greater AOC slab component in these lavas than in the VA. The Buta Ranquil sample near
637 Tromen may have the most AOC slab component which could explain the high $^{143}Nd/^{144}Nd$
638 isotope ratio on Figure 5 and why this sample has the lowest $^{207}Pb/^{204}Pb$ and $^{208}Pb/^{204}Pb$ at a
639 given $^{206}Pb/^{204}Pb$. This sample also plots closer to the AOC end member on Figure 7, 10 and 11
640 than do the other NBA and Tromen samples.
641 Other isotopes are more ambiguous because of the extensive overlap between the mantle
642 and trench sediments. Although Sr and Nd isotopes for a few samples from the northern VA lie
643 within the field defined by BA samples with the least evidence of a slab component (SBA and
644 Pampas Negras), most are displaced to higher Sr but not lower Nd ratios (Figure 5, 12a). This
645 kind of offset is consistent with both elements being derived in part from AOC as well as
646 sediment, and a higher mass fraction of slab component at the VA (Figure 12b). $\delta^{18}O_{olivine}$ is
647 virtually constant across the range of Sr and Pb isotopes (e.g., Figures 6c, 13), indicating that
648 variation in Sr and Pb isotope ratios in rocks as mafic as ours reflects source mixing between

depleted upper mantle and an enriched component, such as sedimentary material or fluids/melts from subducted sediments, rather than crustal assimilation

Hf-Nd isotopes are not helpful in this regard, because there is so much variation within the mantle and the general immobility of Hf and to a lesser extent Nd in most slab components. However, all analyses of Chilean trench sediments from 35°-40°S have $^{143}Nd/^{144}Nd$ ratios overlapping those of the arc, none of the arc rocks are offset toward a more pelagic sediment composition, and a mixture of sediment and AOC may lie within the Hf-Nd VA array. Neither VA nor BA samples define the steep positive correlation between $^{176}Hf/^{177}Hf$ and LREE/Hf ratios that is common in oceanic arcs and can be attributed to addition of LREE > Hf in the slab component (e.g. Todd et al., 2011).

In conclusion, Pb, Sr, and Nd isotopes are most easily explained by mixing with a slab component that includes a significant mass fraction of AOC as well sediment.

(2) Nature of the slab component: solid, fluid, or melt?

The slab component could be added to the overlying mantle wedge via subduction erosion, a fluid derived from the dehydration of the slab (e.g. Elliot et al., 1997), or a melt if the slab temperature exceeds the solidus of sediment (e.g. van Keken et al., 2011) and/or AOC (e.g. Tollstrup et al., 2010). In the previous section, we argued that the Pb isotope data rule out subduction erosion of Paleozoic or older crust. Therefore, fluids and/or melts from the subducting slab, or from a solid diaper carrying sediments and possibly some AOC from the subducting slab (e.g. Hall and Kincaid, 2001; Behn et al., 2011), probably carry the slab component into the mantle wedge beneath the TSVZ. The VA and BA volcanic rocks display an excellent positive correlation between Nb/U and Ce/Pb (r^2 = 0.93), extending from average MORB and OIB values of 45 for Nb/U and 25 for Ce/Pb (Hofmann et al., 1986) in the BA to values of 1 for Nb/U and 2 for Ce/Pb in the VA, which overlap values for trench sediments (Figure 10). The correlation suggests that two components dominate the geochemistry of the TSVZ rocks: a homogeneous slab component rich in fluid-mobile elements, such as Pb and U, and a decompressive partial melt of the mantle wedge that has the usual mantle values for these ratios.

The slab component must also contain Th and LREE, because all VA and NBA samples are displaced above the usual MORB-OIB array in Nb/Yb versus Th/Yb (Figure 11) and La/Yb diagrams (not shown). This rules out a fluid slab component, because Th and LREE partition strongly into the liquid component only at temperatures above the AOC or sediment solidus (Johnson and Plank, 1999; Kessel et al., 2005). Partial melts, on the other hand, can fractionate and transport Th and LREE (Kessel et al., 2005). Moreover, the VA samples overlap the trench sediment in Nb/Yb and extend to higher Th/Yb and La/Yb ratios, which means that the slab component is preferentially enriched in Th and La relative to Yb. Therefore, melting involving equilibrium with minerals such as garnet is required.

Pb isotope ratios (e.g. $^{206}Pb/^{204}Pb$) form good inverse correlations with Nb/Zr ($r^2 = 0.70$), Nb/U ($r^2 = 0.84$), Ce/Pb ($r^2 = 0.81$), and Nb/Ba ($r^2 = 0.75$) (Figure 7, not all ratios shown). Although the latter correlations could be explained by adding a slab-derived fluid to the mantle, it is unlikely that fluid can transport enough Zr to explain the correlation. Instead, we attribute the variation to mixing with a slab-derived melt.

We noted earlier that the Mocha Fracture Zone may project under Longaví. We looked for evidence of greater than usual slab component at Longaví that might result from greater slab hydration at the fracture zone, as proposed by Sellés et al. (2004). However, we found no such evidence. Typical fluid-mobile to fluid-immobile trace elements ratios (e.g. U/Th, Pb/Ce, Ba/Nb, not shown) are relatively constant along this portion of the arc.

In summary, we conclude that the slab component is a melt of both trench sediment and AOC that it is homogenous throughout the TSVZ, and that it is ubiquitous at the VA but less and variable in the BA – most in the NBA and Tromen and least at the SBA. The slab surface temperature beneath the TSVZ VA has been inferred to be ~830^{o}C (van Keken et al., 2011), which is only hot enough to melt AOC and sediment at the depth of the slab beneath the VA under water saturated conditions (Hermann and Spandler, 2008; Klimm et al., 2008). This conclusion is true for most subduction zones and requires a ubiquitous source of water external to any remaining hydrous minerals in the sediment or AOC themselves. Serpentinite in the underlying subducting mantle, possibly produced during bend-faulting at the outer rise (e.g. Contreras Reyes et al., 2007; Grevemeyer et al., 2007; Ranero et al., 2003; Rüpke et al., 2002, 2004), is an obvious candidate for the water source. Bend-faults, which provide deep reaching

pathways, can be observed in the seafloor bathymetry in the incoming plate outboard of the TSVZ (Ranero et al., 2005; Ranero et al., 2006).

D. Quantitative flux melting model.

We quantified some of our arguments by using the Arc Basalt Simulator version 3.10 of Kimura et al. (2009, 2010) to which the reader is referred for full details of the method. Briefly, ABS calculates forward mass balance models for the trace element and isotopic composition of arc basalts using assumed values for input parameters (AOC, sediment, mantle), the local P-T conditions of the slab from Syracuse et al. (2010), temperature-dependent trace element partitioning from Kessel et al. (2005), the integrated dehydration history of the slab from van Keken et al. (2011), and PMELTS-based flux mantle melting from Katz et al. (2003). As in most papers, successful models are subjective judgments about the fit between model prediction and representative basalts for extended trace element patterns and isotope ratios (e.g. Figure 12).

Table 3 and 4 contain: 1) our assumed compositions for the mantle, AOC and sediment; 2) the pressure of the slab surface beneath the volcanic front (4 GPa) from Syracuse and Abers (2009); 3) the temperature of the slab surface at this depth for Central Chile (830^{o}C) from Syracuse et al. (2011); 4) the modal mineralogy of basalt and sediment at these P-T conditions as calculated within ABS using Perple_X, following van Keken et al. (2011); and 5) the percent of water-saturated melting at this P-T (18%) from Hermann and Spandler (2008). Table 4 also gives the bulk partition coefficients for these modal mineralogies for Sr, Nd, and Pb at 830^{o}C that are used for the mixing model in Figure 12. They are based on Kessel et al. (2005) for garnet and clinopyroxene, and Green and Adam (2003) for phengite. D's are assumed to be zero for the SiO_2 phase and rutile except for rutile D_{Nd} = 0.7 (from Ayers and Watson, 1993). Table 3 also gives the P-T-F conditions of melting in the mantle wedge that results in the best match of the shape of the REE pattern of a representative volcanic arc basalt (CL575 from San Pedro), and the corresponding bulk partition coefficients based on Green et al. (2000). At these P-T conditions, each percent of slab melt added to the mantle results in about one percent of mantle melting based on Katz et al. (2003). Between 0.5-1.5% slab melt yields the best match for most trace elements and isotopes (Figure 12), and the resulting primitive basalts contain about 3 wt. % water. ABS version 3 does not include the sequential effects of dehydration in all layers of the

slab or residual accessory minerals besides rutile. Although our model is only heuristic, predicted and observed isotope ratios agree well, and trace element concentrations agree to within 10-20% for most elements except for Ba and U that are over-predicted, perhaps because of the sediment values assumed.

Although this approach is easier for a homogeneous mantle, we adapted it for the heterogeneity that we infer for the TSVZ VA by using two South Atlantic MORB type mantle compositions -- Depleted (SAM-D) and Enriched (SAM-E) -- that bracket the VA samples in Sr, Nd, and Pb isotopes. We assume that SAM-D and SAM-E have the trace element concentrations of the DMM and E-DMM of Workman and Hart (2005), respectively. However, the difference in concentrations between N-MORB and E-MORB sources has no effect on the mixing model because the slab melts are so much more enriched than the mantle wedge.

We also assumed a uniform slab component derived from both sediment and AOC for reasons given earlier. A sediment:AOC ratio of 60:40 gave the most satisfactory results but we have little independent control for this parameter. The isotopic composition of the sediment in Table 3 is from Lucassen et al. (2010) and the trace element composition is from our sample SO210-#5-B as explained earlier. The AOC composition is from ODP Site 1149 in the western Pacific (Kelley et al., 2003; Hauff et al., 2003) as compiled by Tollstrup et al. (2010).

Figure 12 shows the Sr-Nd-Pb isotope ratios for the resulting mixtures. They bracket all the Sr-Nd-Pb isotope data for the TSVZ when 0.5-1% of slab component is added to the depleted to enriched mantles except for two northern VA samples requiring 2-3% slab component. The separation between VA and BA is greater for Pb than Sr-Nd isotopes. A mixed-source slab component, slab melting, and a heterogeneous mantle all are required. Little or no slab component is needed for Sr and Nd in the SBA and Pampas Negras BA and Resolana/Los Hornitos VA basalts, but some slab-derived Pb is necessary for Resolana/Los Hornitos. Assuming an average $\delta^{18}O$ value of 9‰ for sediment (Table 2) plus 2‰ (for hydrothermally-altered lower AOC) and 5.25‰ (for mantle wedge) (see Bindeman et al., 2005, and references therein), the model shown in Figure 13 predicts little if any change in O isotopes from the slab contribution to the VA mantle source.

Although some volcanic centers and regions define slopes that are shallower than the mixing lines, we attribute this to the heuristic generality of our model. All mixing components are likely to be heterogeneous in an area as large as this. Local variations in the isotopic

771 composition of the mantle or subducted sediment or both, and in the P-T conditions of the slab
772 component, all will affect the slope of mixing lines in Figure 12. For example, two samples (CL
773 323/CL 325) plot close to SAM-E on the Sr versus Nd isotope diagram (Figure 12a) but seem to
774 mix to SAM-D on the Sr versus Pb isotope diagram (Figure 12b). More generally, our model
775 predicts slightly more slab component when using Pb isotopes than when using Nd isotopes.
776 This may reflect a more fluid-like slab component with higher Pb/Nd than the melt calculated
777 using ABS3.10. Our model could be fine-tuned to any subset of samples but our goal is to create
778 a framework with which such tuning can start.
779
780 **E. Regional and global comparisons**
781
782 Although lying on relatively thick continental crust (ca. 40 km), the TSVZ differs from
783 the CVZ in Peru and northern Chile (14-27°S) where the crust is ca. 70 km thick. There, crustal
784 contamination plays a fundamental role in the magma genesis (e.g. Davidson et al., 1991, Francis
785 and Hawkesworth, 1994, Lindsay et al., 2001b, Schmitt et al., 2001, 2002). In the CVZ, Sr, Nd
786 and O isotopes correlate with increasing SiO_2 content, and Pb isotopes show correlations with
787 the local Andean basement (e.g. Francis et al., 1984; Feeley and Davidson, 1994, Wörner et al.,
788 1992b, 1994; Aitcheson et al., 1995). The TSVZ also differs from the NSVZ where the crust is
789 also thick but where enriched Sr-Nd isotopic compositions have been observed and interpreted as
790 the result of either crustal assimilation (Hildreth and Moorbath, 1988) or subduction erosion
791 (Kay et al., 2005). Our TSVZ study reaches different conclusions about the crustal influence than
792 previous large-scale studies (e.g. Hildreth and Moorbath, 1988, Tormey et al., 1991) or single-
793 volcano studies (e.g. Dungan et al., 2001, Tormey et al., 1995) because we found no correlations
794 between isotopes and differentiation indices and no mixing of Pb isotopes toward the local
795 basement. Our O isotope data also show a typical subduction zone signature within and slightly
796 above the mantle range.
797 Instead, the sediment-dominated slab component in the TSVZ is a feature more similar to
798 the CSVZ to the south. There, previous studies have shown that basalts were formed by melting
799 of the subarc mantle contaminated by fluids derived from the dehydration of the subducting
800 oceanic lithosphere including sediments (e.g. Morris et al., 1990, Sigmarsson et al., 1990, 2002,
801 Hickey-Vargas et al., 1984, 1986, 1989, 2002). However, we conclude that both the subducting

802 oceanic crust and the sediments melt. Our conclusion that the mass fraction of slab component
803 and the degree of mantle melting both decrease eastward into the back arc agrees with previous
804 studies (e.g. Futa and Stern, 1988, Hickey-Vargas et al., 1986, 1989).
805 While most previous studies of the TSVZ showed a transition between a slab component
806 in the CSVZ and a crustal component in the NSVZ, we show rather than the TSVZ segment can
807 be interpreted as a "baseline" of subduction input, and that the mantle wedge is heterogeneous in
808 its trace element and isotope ratios.
809
810 **F. Conclusions:**
811
812 We use new major and trace element and Sr-Nd-Hf-Pb-O isotope data for basalts from
813 the volcanic arc and backarc of the Transitional Southern Volcanic Zone (34.4°S-38°S) of Chile,
814 and adjacent trench sediments, to evaluate the origin of the arc magmas. We conclude the
815 following.
816 (1) Major assimilation of pre-Cenozoic sialic crust is inconsistent with our isotopic data
817 for basalts to andesites despite their ascent through 35-45 km thick crust.
818 (2) The mantle is heterogeneous within and between the volcanic arc and backarc. The
819 range is similar to the South Atlantic MORB field in Sr and Nd, but not in Pb and Hf
820 isotopes. Mixing between a slab component and South Atlantic MORB can explain
821 the Pb isotope data. Pb isotopes in the VA, NBA, and Tromen are dominated by
822 subducting sediments. We attribute the difference between VA and BA in Hf isotopes
823 to the presence of subcontinental lithosphere beneath the backarc, but cannot
824 constrain if it is presently located within the lithospheric mantle or has been
825 delaminated and is presently in the asthenospheric mantle wedge.
826 (3) All samples from the volcanic arc, and most from the backarc, contain a slab-derived
827 component. The mass fraction of this component is less in the backarc and negligible
828 in the SBA basalts farthest from the volcanic arc.
829 (4) The slab component is homogeneous and drawn from subequal amounts of subducted
830 sediment and altered oceanic crust. It must be a melt in order to transport Th, Zr and
831 LREE, and to fractionate them so much from HREE. For melting to occur at the
832 depth of the slab beneath the volcanic arc, the slab must be water-saturated at least

locally, which requires an external source of water such as from dehydrating underlying serpentinite within the subducting plate, possibly formed through the access of water into the uppermost lithospheric mantle as a result of bend-faulting preceeding subduction.

(5) Trace element patterns and Sr-Nd-Pb isotope ratios are best modelled by adding 0.5-1% of a slab melt (except for two rear arc samples which require 2-3% slab melt) derived from a 60:40 sediment:AOC source to slightly depleted and isotopically heterogeneous mantle.

(6) Addition of a few percent of this slab component causes an equivalent amount of melting of the mantle at about 2 GPa beneath the VA, with more melting beneath the volcanic arc than backarc. This is consistent with the larger magma flux observed at the volcanic arc.

Acknowledgements:

We thank U. Westernströer and S. Hauff for their analytical help. We thank the Federal Ministry of Education and Research (BMBF) for funding the R/V SONNE during the SO210 cruise. Ilya N. Bindeman acknowledges NSF grants EAR-0844772 and EAR-0948455. We thank three anonymous reviewers who helped to increase the quality of this paper. This paper is contribution No. 259 of Collaborative Research Center (Sonderforschungsbereich) SFB574 "Volatiles and Fluids in subduction Zones" at Kiel University, funded by the German Research Foundation

References Cited:

Amante C. and Eakins B.W. (2009) ETOPO1 1 Arc-Minute Global Relief Model: Procedures, Data sources and Analysis, NOAA Technical Memorandum NESDIS NGDC-24, 19pp

Andres M., Blichert-Toft J. and Schilling J.G. (2002) Hafnium isotopes in basalts from the Southern Mid-Atlantic Ridge from 40° to 55°S: Discovery and Shona plume-Ridge interactions and the role of recycled sediments, *Geochemistry Geophysics Geosystems* **3**

Auer S., Bindeman I.N., Wallace P., Ponomareva V. and Portnyagin M. (2009) The origin of hydrous, high-$\delta^{18}O$ voluminous volcanism: diverse oxygen isotope values and high

magmatic water contents within the volcanic record of Klyuchevskoy volcano, Kamchatka, Russia, *Contributions to Mineralogy and Petrology* **157**, 209-230

Angermann D., Klotz J. and Reigber C. (1999) Space geodetic estimation of the Nazca-South America Euler vector, *Earth and Planetary Science Letters* **171**, 329-334

Ayers and Watson (1993) Rutile solubility and mobility in supercritical aqueous fluids, *Contributions to Mineralogy and Petrology* **114**, 321-330

Behn M.D., Kelemen P.B., Hirth G., Hacker B.R. and Massonne H.-J. (2011) Diapirs as the source of the sediment signature in arc lavas, *Nature Geosciences* **4**, 641-646

Bertotto G.W., Cingolani C.A. and Bjerg E.A. (2009) Geochemical variations in Cenozoic back-arc basalts at the border of La Pampa and Mendoza provinces, Argentina, *Journal of South American Earth Sciences* **28**, 360-373

Bindeman I.N., Ponomareva V.V., Bailey J.C. and Valley J.W. (2004) Volcanic arc of Kamchatka: a province with high-$\delta^{18}O$ magma sources and large scale $^{18}O/^{16}O$ depletion of the upper crust, *Geochimica et Cosmochimica Acta* **68**, 841-865

Bindeman I.N., Eiler J.M., Yogodzinski G.M., Tatsumi Y., Stern C.R., Grove T.L., Portnyagin M., Hoernle K. and Danyushevsky L.V. (2005) Oxygen isotope evidence for slab melting in modern and ancient subduction zones, *Earth and Planetary Science Letters* **235**, 480-496

Bindeman I.N. (2008) Oxygen isotopes in mantle and crustal magmas as revealed by single crystal analysis, *Reviews in Mineralogy and Geochemistry* **69**, 445-478

Blichert-Toft J. and Albarède F. (1997) The Lu-Hf isotope geochemistry of chondrites and the evolution of the mantle-crust system, *Earth and Planetary Science Letters* **148**, 243-258

Burd A., Booker J.R., Pomposielle M.C., Favetto A., Larsen J., Giordanengo G. and Orozco Bernal L. (2008) Electrical conductivity beneath the Payún Matrú volcanic field in the Andean back-arc of Argentina near 36.5°S: insights into the magma source, 7th International symposium on Andean Geodynamics (Nice), Extended abstracts, 90-93

Cembrano J. and Lara L.E. (2009) The link between volcanism and tectonics in the southern volcanic zone of the Chilean Andes: a review, *Tectonophysics* **471**, 96-123

Contreras-Reyes E., Grevemeyer I., Flueh E.R., Scherwath M. and Heesemann M. (2007) Alteration of the subducting oceanic lithosphere at the southern central Chile trench-outer rise, *Geochemistry Geophysics Geosystems* **8**

Contreras-Reyes E., Grevemeyer I., Flueh E.R. and Reichert C. (2008) Upper lithospheric structure of the subduction zone offshore of southern Arauco peninsula, Chile, at ~38°S, *Journal of Geophysical Research* **113**

Davidson J.P., Dungan M.A. , Ferguson K.M. and Colucci M.T. (1987) Crust-magma interactions and the evolution of arc magmas : The San Pedro-Pellado volcanic complex, southern Chilean Andes, *Geology* **15**, 443-446

Davidson J.P., Ferguson K.M., Colucci M.T. and Dungan M.A. (1988) The origin and evolution of magmas from the San Pedro-Pellado volcanic complex, S. Chile: multicomponent sources and open system evolution, *Contributions to Mineralogy and Petrology* **100**, 429-445

Douglass J., Schilling J.G. and Fontignie D. (1999) Plume-ridge interactions of the Discovery and Shona mantle plumes with the Southern mid-Atlantic ridge (40-55 degree South), *Journal of Geophysical Research* **104**, 2941-2962

Douglass J. (2002) Isotopic and trace element variations along the Southern Mid-Atlantic Ridge (40-50°S): An evaluation of regional plume-ridge interaction and large-scale mantle heterogeneities, Ph.D. thesis, Univ. of Rhode Island, Kingston, R.I.

Dungan M.A., Wulff A. and Thompson R. (2001) Eruptive stratigraphy of the Tatara-San Pedro complex, 36°S, Southern Volcanic Zone, Chilean Andes: reconstruction method and implications for magma evolution at long-lived arc volcanic centers, *Journal of Petrology* **42**, 555-626

Dungan M.A. and Davidson J.P. (2004) Partial assimilative recycling of the mafic plutonic roots of arc volcanoes: an example from the Chilean Andes, *Geology* **32**, 773-776

Eiler J.M., Carr M.J., Reagan M. and Stolper E. (2005) Oxygen isotope constraints on the sources of Central American arc lavas, *Geochemistry Geophysics Geosystems* **6**

Elliot T., Plank T., Zindler A., White W. and Bourdon B. (1997) Element transport from slab to volcanic front at the Mariana arc, *Journal of Geophysical Research* **102**, 14991-15019

Ewart A. and Hawkesworth C.J. (1987) The Pleistocene-Recent Tonga-Kermadec arc lavas: Interpretation of new isotopic and Rare Earth data in terms of Depleted Mantle source model, *Journal of Petrology* **28**, 495-530

Folguera A., Naranjo J.A., Orihashi Y., Sumino H., Nagao K., Polanco E. and Ramos V.A. (2009) Retroarc volcanism in the northern San Rafael Block (34°-35°30S), southern

926 Central Andes: Occurrence, age, and tectonic setting, *Journal of Volcanology and*
927 *Geothermal Research* **186**, 169-185
928 Fontignie D. and Schilling J.G. (1991) $^{87}Sr/^{86}Sr$ and REE variations along the Easter microplate
929 boundaries (South Pacific): application of multivariate statistical analyses to ridge
930 segmentation, *Chemical Geology* **89**, 209-241
931 Fontignie D. and Schilling J.G. (1996) Mantle heterogeneities beneath the South Atlantic : a Nd-
932 Sr-Pb isotopes study along the mid-Atlantic ridge (3 degree South-46 degree South), *Earth*
933 *and Planetary Science Letters* **142**, 209-221
934 Futa K. and Stern C.R. (1988) Sr and Nd isotopic and trace element compositions of Quaternary
935 volcanic centers of the Southern Andes, *Earth and Planetary Sciences Letters* **88**, 253-262
936 Garbe-Schönberg C.-D. (1993)Simultaneous determination of thirty-seven trace elements in
937 twenty-eight international rocks standards by ICP-MS, *Geostandards Newsletter* **17**, 81-97
938 Geldmacher J.R. and Hoernle K. (2006) Origin and geochemical evolution of the Madeira-Tore
939 Rise (eastern North Atlantic), *Journal of Geophysical Research* **111**
940 Gilbert H., Beck S. and Zandt G. (2006) Lithospheric and upper mantle structure of central Chile
941 and Argentina, *Geophysical Journal International* **165**
942 Gill J.B. (1981) Orogenic andesites and plate tectonics, Berlin, Heidelberg, New York, Tokyo,
943 Springer, 390p
944 Govindaraju K. (1994) Compilation of working values and sample description for 383
945 geostandards, *Geostandards Newsletter* **18**, 1-158
946 Green T.H., Blundy J.D., Adam J. and Yaxley G.M. (2000) SIMS determination of trace element
947 partition coefficients between garnet, clinopyroxene, and hydrous basaltic liquids at 2-7.5
948 GPa and 1080-1200°C, *Lithos* **53**, 165-187
949 Green T.H. and Adam J. (2003) Experimentally determined trace element characteristics of
950 aqueous fluid from partially dehydrated mafic oceanic crust at 3.0 GPa, 650-700°C,
951 *European Journal of Mineralogy.* **15**, 815-830
952 Grevemeyer I., Ranero C.R., Flueh E.R., Kläschen D. and Bialas J. (2007) Passive and active
953 seismological study of bending-related faulting and mantle serpentinization at the Middle
954 America trench, *Earth and Planetary Science Letters* **258**, 528-542

955 Gudnason J., Martin Holm P., Søager N. and Llambías E.J. (2012) Geochronology of the late
956 Pliocene to recent volcanic activity in the Payenia back-arc volcanic province, Mendoza
957 Argentina, *Journal of South American Earth Sciences* **37**, 191-201
958 Haase K.M. (2002) Geochemical constraints on magma sources and mixing processes in Easter
959 microplate MORB (SE Pacific); A case study of plume-ridge interaction, *Chemical*
960 *Geology* **182**, 335-355
961 Hall P.S. and Kincaid C. (2001) Diapiric flow at subduction zones: A recipe for rapid transport,
962 *Science* **292**, 2472
963 Hamelin B., Dupré B. and Allègre C.J. (1984) Lead-Strontium isotopic variations along the East
964 Pacific Rise and the Mid-Atlantic Ridge: a comparative study, *Earth and Planetary*
965 *Science Letters* **67**, 340-350
966 Hanan B.B., Kingsley R.H. and Schilling J.G. (1986) Pb isotope evidence in the South Atlantic
967 for migrating ridge-hot spots interactions, *Nature* **322**, 137-144
968 Hanan B.B. and Schilling J.G. (1989) Easter microplate evolution: Pb isotope evidence, *Journal*
969 *of Geophysical Research* **94**, 7432-7448
970 Harmon R.S., Barreiro B.A., Moorbath S., Hoefs J., Francis P.W., Thorpe R.S., Deruelle B.,
971 McHugh J. and Viglino J.A. (1984) Regional O-, Sr-, and Pb-isotopes relationships in late
972 Cenozoic calc-alkaline lavas of the Andean cordillera, *Journal of Geological Society*
973 *London* **141,** 803
974 Hauff F., Hoernle K. And Schmidt A. (2003) Sr-Nd-Pb composition of Mesozoic Pacific oceanic
975 crust (Site 1149 and 801, ODP Leg 185): Implications for alteration of ocean crust and the
976 input into the Izu-Bonin-Mariana subduction system, *Geochemistry Geophysics*
977 *Geosystems* **4**
978 Hermann J. and Spandler C.J. (2008) Sediment melts at sub-arc depths: an experimental study,
979 *Journal of Petrology* **49**, 717-740
980 Herron E.M., Cande S.C. and Hall B.R. (1981) An active spreading center collides with a
981 subduction zone – a geophysical survey of the Chile margin triple junction, *Geological*
982 *Society of America Memoirs* **154**, 683-701
983 Heydolph K., Hoernle K., Hauff F., van den Bogaard P., Portnyagin M., Bindeman I. and Garbe-
984 Schönberg C.-D. (2012) Along- and across-arc geochemical variations in nortwestern
985 Central America: Increased contribution of enriched lithosphere to lavas along the

986 volcanic from Nicaragua to Guatemala and behind the volcanic front, *Geochimica et*
987 *Cosmochimica Acta* **84**, 459-491
988 Hickey R.L., Gerlach D.C. and Frey F.A. (1984) Geochemical variations in volcanic rocks from
989 central-south Chile (33°-42°S): Implications for their petrogenesis In Andean magmatism:
990 Chemical and isotopic constraints (Harmon R. Barreiro B., editors). Shiva Publishing
991 Limited p. 72-95 Nantwich, U.K.
992 Hickey R.L., Frey F.A. and Gerlach D.C. (1986) Multiple sources for basaltic arc rocks from the
993 Southern Volcanic Zone of the Andes (34°-41°S): Trace element and isotopic evidence for
994 contributions from subducted oceanic crust, mantle, and continental crust, *Journal of*
995 *Geophysical Research* **91**, 5963-5983
996 Hickey-Vargas R.L., Moreno Roa H., Lopez-Escobar L. and Frey F.A. (1989) Geochemical
997 variations in Andean basaltic and silicic lavas from the Villarrica-Lanin volcanic chain
998 (39.5°S): an evaluation of source heterogeneity, fractional crystallization and crustal
999 assimilation, *Contributions to Mineralogy and Petrology* **103**, 361-386
1000 Hickey-Vargas R.L., Sun M., Lopez-Escobar L., Moreno Roa H., Reagan M.K., Morris J.D. and
1001 Ryan J.G. (2002) Multiple subduction components in the mantle wedge: Evidence from
1002 eruptive centers in the Central Southern volcanic zone, Chile, *Geology* **30**, 3, 199-202
1003 Hildreth W. and Moorbath S. (1988) Crustal contributions to arc magmatism in the Andes of
1004 Central Chile, *Contributions to Mineralogy and Petrology* **98**, 455-489
1005 Hildreth W., Godoy E., Fierstein J. and Singer B. (2010) Laguna del Maule Volcanic Field:
1006 Eruptive history of a Quaternary basalt-to-rhyolite distributed field on the Andean
1007 rangecrest in central Chile, *Servicio Nacional de Geologia y Mineria Boletin* **63**, 145p
1008 Hochstaedter A., Gill J.B., Peters R., Broughton P., Holden P. and Taylor B. (2001) Across-arc
1009 geochemical trends in the Izu-Bonin arc: contributions from the subducting slab,
1010 *Geochemistry Geophysics Geosystems* **2**
1011 Hoernle K., Abt D.L., Fisher K.M., Nichols H., Hauff F., Abers G.A., van den Bogaard P.,
1012 Heydolph K., Alvarado G., Protti M., Strauch W. (2008) Arc parallel flow in the mantle
1013 wedge beneath Costa Rica and Nicaragua, *Nature* **451**, 1094-1097
1014 Hoernle K., Hauff F., Kokfelt T.F., Haase K., Garbe-Schönberg C.-D. and Werner R. (2011) On-
1015 and off-axis chemical heterogeneities along the South Atlantic Mid-Ocean Ridge (5-

11°S): Shallow or deep recycling of ocean crust and/or intraplate volcanism? *Earth and Planetary Science Letters* **306**, 86-97

Hofmann A.W., Jochum K.P., Seufert M. and White W.M. (1986) Nb and Pb in oceanic basalts: new constraints on mantle evolution, *Earth and Planetary Sciences letters* **79**, 33-45

Husson L., Conrad C.P. and Faccenna C. (2012) Plate motions, Andean orogeny, and volcanism above the South Atlantic convection cell, *Earth and Planetary Sciences Letters* **317-318**, 126-135

Ito E., White W.M., von Drach V., Hofmann A.W. and James D.E. (1980) Isotopic studies of ocean ridge basalts, Carnegie Institute, DTM, annual report director, 465-471

Ito E., White W.M. and Goepel C. (1987) The O, Sr, Nd and Pb isotope geochemistry of mid-oceans ridge basalts, *Chemical Geology* **62**, 157-176

Johnson M.C. and Plank T. (1999) Dehydration and melting experiments constrain the fate of subducted sediments, *Geochemistry Geophysics Geosystems* **1**, 1007-1033,

Katz R.F., Spiegelman M. and Langmuir C.H. (2003) A new parameterization of hydrous mantle melting, *Geochemistry Geophysics Geosystems* **4**, 1073-1092

Kay S.M., Gorring M. and Ramos V.A. (2004) Magmatic sources, setting and causes of Eocene to recent Patagonian plateau magmatism (36° to 52°S latitude), *Revista de la Asociación Geológica Argentina* **59**, 556-568, 2004

Kay S.M., Godoy E. and Kurtz A. (2005) Episodic arc migration, crustal thickening, subduction erosion, and magmatism in the south-central Andes, *Geological Society of America* **117**, 67-88

Kay S.M., Burns W.M., Copeland P. and Mancilla O. (2006a) Upper Cretaceous to Holocene magmatism and evidence for transient Miocene shallowing of the Andean subduction zone under the northern Neuquén Basin, *Geological Society of America* Special Paper **407**, 19-60

Kay S.M. and Copeland P. (2006b) Early to middle Miocene backarc magmas of the Neuquén Basin: geochemical consequences of slab shallowing and westward drift of South America, *Geological Society of America* Special Paper **407,** 185-214, 2006b

Kay S.M., Mancilla O. and Copeland P. (2006c) Evolution of the late Miocene Chachahuén volcanic complex at 37°S over a transient shallow subduction zone under the Neuquén Andes, *Geological Society of America* Special Paper **407**, 215-246

1047 Kessel R., Schmidt M.W., Ulmer P. and Pettke T. (2005) Trace element signature of subduction-
1048 zone fluids, melts and supercritical liquids at 120-180 km depth, *Nature* **437**, 724-727
1049 Kelley K.A., Plank T., Ludden J. and Staudigel H. (2003) Composition of altered oceanic crust at
1050 ODP Sites 801 and 1149, *Geochemistry Geophysics Geosystems* **4**
1051 Kelley K.A., Plank T., Grove T.L., Stolper E.M., Newman S. and Hauri E. (2006) Mantle
1052 melting as a function of water content beneath back-arc basins, *Journal of Geophysical*
1053 *Research* **111**
1054 Kimura J.-I., van Keken P.E., Hacker B.R., Kawabata H., Yoshida T. and Stern R.J. (2009) Arc
1055 Basalt Simulator version 2, a simulation for slab dehydration and fluid-fluxed mantle
1056 melting for arc basalts: Modeling scheme and implication, *Geochemistry Geophysics*
1057 *Geosystems* **10**
1058 Kimura J.-I., Kent A.J.R., Rowe M.C., Katakuse M., Nakano F., Hacker B.R., van Keken P.E.,
1059 Kawabata H. and Stern R.J. (2010) Origin of cross-chain geochemical variation in
1060 Quaternary lavas from the northern Izu arc: Using a quantitative mass balance approach to
1061 identify mantle sources and mantle wedge processes, *Geochemistry Geophysics*
1062 *Geosystems* **11**
1063 Kinglsey R.H. (2002) The geochemistry of basalts from the Easter Microplate boundaries and
1064 the western Easter-Salas y Gomez Seamount Chain: A comprehensive study of mantle
1065 plume-spreading center interaction, Ph.D. thesis, Univ. of Rhode Island, Kingston, R.I.
1066 Kingsley R.H., Blichert-Toft J., Fontignie D. and Schilling J.G. (2007) Hafnium, Neodymium
1067 and Strontium isotope and parent-daughter element systematic in basalts from the plume-
1068 ridge interaction system of the Salas y Gomes seamount chain and Easter microplate,
1069 *Geochemistry Geophysics Geosytems* **8**
1070 Klimm K., Blundy J.D. and Green T.H. (2008) Trace element partitioning and accessory phase
1071 saturation during H_2O-saturated melting of basalt with implications for subduction zone
1072 chemical fluxes, *Journal of Petrology* **49**, 523-553
1073 Krolikowska-Ciaglo S., Hauff F. and Hoernle K. (2005) Sr-Nd isotope systematics in 14–28 Ma
1074 low-temperature altered mid-ocean ridge basalt from the Australian Antarctic
1075 Discordance, Ocean Drilling Program Leg 187, *Geochemistry Geophysics Geosystems* **6**

1076 Le Maitre R.W., Bateman P., Dudek A., Keller J., Lameyre Le Bas M.J., Sabine P.A., Schmid
1077 R., Sorensen H., Streckeisen A., Woodley A.R. and Zanettin B. (1989) A classification of
1078 igneous rocks and glossary of terms, Blackwell, Oxford
1079 Linke P. and Shipboard Scientific Party (2011) CHIFLUX – Identification and investigation of
1080 fluid flux, mass wasting and sediments in the forearc of the central Chilean subduction
1081 zone, Cruise Report SO210, 103 pp., GEOMAR report, Kiel
1082 López-Escobar L., Cembrano J. and Moreno H. (1995) Geochemistry and tectonics of the
1083 Chilean Southern Andes basaltic Quaternary volcanism (37-46°S), *Revista Geológica de*
1084 *Chile* **22**, 219-234
1085 Lucassen F., Trumbull R., Franz G., Creixell C., Vásquez P., Romer R.L. and Figeroa O. (2004)
1086 Distinguishing crustal recycling and juvenile additions at active continental margins : the
1087 Paleozoic to recent compositional evolution of the Chilean Pacific margin (36-41°S),
1088 *Journal of South American Earth Sciences* **17**, 103-119
1089 Lucassen F., Wiedicke M. and Franz G. (2010) Complete recycling of a magmatic arc : evidence
1090 from chemical and isotopic composition of Quaternary trench sediments in Chile (36-
1091 40°S), *International Journal of Earth Sciences* **99**, 687-701
1092 MacDougall J.D. and Lugmair G.W. (1986) Sr and Nd isotopes in basalts from the East Pacific
1093 Rise: significance for mantle heterogeneity, *Earth and Planetary Science letters* **77**, 273-
1094 284
1095 Mahoney J.J., Sinto J.M., Kurz M.D., MacDougall J.D., Spencer K.J. and Lugmair G.W. (1994)
1096 Isotope and trace element characteristics of a super-fast spreading ridge: East Pacific Rise
1097 13-23°S, *Earth and Planetary Science Letters* **121**, 171-191
1098 Martin E., Bindeman I.N. and Grove T.L. (2011) The origin of high-Mg magmas in Mt Shasta
1099 and Medicine lake volcanoes, Cascade arc (California): higher and lower than mantle
1100 oxygen isotope signatures attributed to current and past subduction, *Contributions to*
1101 *Mineralogy and Petrology* **162**
1102 Mattey D., Lowry D. and Macpherson C. (1994) Oxygen isotope composition of mantle
1103 peridotite, *Earth and Planetary Science Letters* **128**, 231-241
1104 Morris J.D., Leeman W.P. and Tera F. (1990) The subducted component in island arc lavas
1105 constraints from Be isotopes and B-Be systematics, *Nature* **344**, 31-36

Mix A.C., Tiedemann R., Blum P. et al. (2003) Proceedings of the Ocean Drilling program, Initial Report **202**

Munoz J. and Stern C.R. (1988) The Quaternary volcanic belt of the southern continental margin of South America: transverse structural and petrochemical variations across the segment between 38°S and 39°S, *Journal of South American Earth Sciences* **1**, 147-161

Naranjo J.A. and Stern C.R. (2004) Holocene tephrochronology of the southernmost part (42°30'-45°S) of the Andean Southern Volcanic Zone, *Revista Geológica de Chile* **31**, 225-240

Newsom H.E., White W.M., Jochum K.P. and Hofmann A.W. (1986) Siderophile and chalcophile element abundances in oceanic basalts, Pb isotopes evolution and growth of the Earth's core, *Earth and Planetary Science Letter* **80**, 299-313

Norabuena E., Leffer-Griffin L., Mao A., Dixon T., Stein S., Sacks S., Ocola L. And Ellis M. (1998) Space geodetic observations of Nazca-South America convergence across the central Andes, *Science* **279**, 358-362

Pearce J.A., Kempton P.D., Nowell G.M. and Noble S.R. (1999) Hf-Nd element and isotope perspective on the nature and provenance of mantle and subduction components in Western Pacific arc-basin systems, *Journal of Petrology* **40**, 1579-1611

Pearce J.A. (2008) Geochemical fingerprinting of oceanic basalts with applications to Ophiolite classification and the search for Archean oceanic crust, *Lithos* **100**, 14-48

Plank T. (2011) The chemical composition of subducting sediments, Chapter for Treatise on Geochemistry

Potts P.J. and Kane J.S. (2005) International association of geoanalysts – Certificate of analysis : Certified reference material OU-6 (penrhyn slate), *Geostandards and Geoanalytical Research* **29**, 233-236

Ramos V.A. and Folguera A. (2011) Payenia volcanic province in the Southern Andes: an appraisal of an exceptional Quaternary tectonic setting, *Journal of Volcanology and Geothermal Research* **201**, 53-64

Ranero C.R., Phipps Morgan J., McIntosh K. and Reichert C. (2003) Bending-related faulting and mantle serpentinization at the Middle America trench, *Nature* **425**, 367-373

1135 Ranero C.R., Villasenor A., Phipps Morgan J. and Weinrebe W. (2005) Relationship between
1136 bend-faulting at trenches and intermediate-depth seismicity, *Geochemistry Geophysics*
1137 *Geosystems* **6**
1138 Ranero C.R., Huene R.v., Weinrebe W. and Reichert C. (2006) Tectonic Processing along the
1139 Chile Convergent Margin, In: O. Oncken, G. Chong, G. Franz, P. Giese, H.-J. Götze, V.
1140 Ramos M. Strecker, and P. Wigger (Eds): The Andes Active Subduction Orogeny,
1141 Frontiers in Earth Science. Springer Verlag, Berlin, 91-121
1142 Roy-Barman M., Wasserburg G.J., Papanastassiou D.A. and Chaussidon M. (1998) Osmium
1143 isotopic compositions and Re-Os concentrations in sulfide globules from basaltic glasses,
1144 *Earth and Planetary Science Letters* **154**, 331-347
1145 Rüpke L.H., Phipps Morgan J., Hort M. and Connolly J.A.D. (2002) Are the regional variations
1146 in Central American arc lavas due to differing basaltic versus peridotitic slab sources of
1147 fluids?, *Geology* **30**, 1035-1038
1148 Rüpke L.H., Phipps Morgan J., Hort M. and Connolly J.A.D. (2004) Serpentine and the
1149 subduction zone water cycle, *Earth and Planetary Science Letters* **223**, 17-37
1150 Sellés D., Ródriguez A.C., Dungan M.A, Naranjo J.A. and Gardeweg M. (2004) Geochemistry
1151 of Neva de Longaví volcano (36.2°S): a compositionally atypical arc volcano in the
1152 Southern Volcanic Zone of the Andes, *Revista Geológica de Chile* **31**, 293-315
1153 Sigmarsson O., Condomines M., Morris J.D. and Harmon R.S. (1990) Uranium and 10be
1154 enrichments by fluids in Andean arc magmas, *Nature* **346**, 163-165
1155 Sigmarsson O., Chmeleff J., Morris J. and López-Escobar L. (2002) Origin of 226Ra-230^{Th}
1156 disequilibria in arc lavas from southern Chile and implications for magma transfer time,
1157 *Earth and Planetary Science Letters* **196**, 189-196
1158 Stern C.R. (1989) Pliocene to present migration of the volcanic front, Andean Southern Volcanic
1159 Front, *Revista Geológica de Chile* **16**, 145-162
1160 Stern C.R. (1991) Role of subduction erosion in the generation of andean magmas, *Geology* **19**,
1161 78-81
1162 Stern C.R. (2004) Active Andean volcanism: its geologic and tectonic setting, *Revista Geológica*
1163 *de Chile* **31**, 161-206
1164 Sun S.-S. and McDonough W.F. (1989) Chemical and isotopic systematic of oceanic basalts :
1165 implications for mantle composition and processes, in Magmatism in ocean basins

(Saunders A.D. and Norry M.J., editors) Geological Society, London special publication **42**, 313-345

Syracuse E.M. and Abers G.A. (2009) Systematic biases in subduction zone hypocenters, *Geophysical Research Letters* **36**

Syracuse E.M., van Keken P.E. and Abers G.A. (2010) The global range of subduction zone thermal models, *Physics of the Earth and Planetary Interiors* **183**(1-2), 73-90

Tassara A., Götze H.J., Schmidt S. and Hackney R. (2006) Three-dimensional density model of the Nazca plate and the Andean continent margin, *Journal of Geophysical Research* **111**

Tebbens S.F. and Cande S.C. (1997a) Southeast Pacific tectonic evolution from early Oligocene to present, *Journal of Geophysical Research* **102**, 12,061-12,084

Tebbens S.F., Cande S.C., Kovacs L., Parra Labrecque J.L. and Vergara H. (1997b) The Chile ridge: a tectonic framework, *Journal of Geophysical Research* **102**, 12,035-12,059

Todd E., Gill J.B., Wysoczanski R.J., Hergt J., Wright I.C., Leybourne M.I. and Mortimer N. (2011) Hf isotopic evidence for small-scale heterogeneity in the mode of mantle wedge enrichment: Southern Havre Trough and South Fiji Basin back arcs, *Geochemistry Geophysics Geosystems* **12**, 34pp

Tollstrup D. and Gill J.B. (2005) Hafnium systematics of the Mariana arc: Evidence for sediment melt and residual phases, *Geology* **33**, 737-740

Tollstrup D., Gill J.B., Kent A., Prinkey D., Williams R., Tamura Y. and Ishizuka O. (2010) Across-arc geochemical trends in the Izu-Bonin arc: Contributions from the subducting slab, revisited, *Geochemistry Geophysics Geosystems* **11**,

Tormey D.R., Hickey-Vargas R., Frey F.A. and López-Escobar L. (1991) Recent lavas from the Andean volcanic front (33 to 42°S); Interpretations of along-arc compositional variations, *Geological Society of America* special paper **265**, 57-77

Tormey D.R., Frey F.A. and Lopez-Escobar L. (1995) Geochemistry of the Active Azufre—Planchón—Peteroa Volcanic Complex, Chile (35°15′S): Evidence for Multiple Sources and Processes in a Cordilleran Arc Magmatic System, *Journal of Petrology* **36**, 265-298

Turner S., Handler M., Bindeman I.N. and Katsuhiko S. (2009) New insights into the origin of O-Hf-Os signatures in arc lavas from Tonga-Kermadec, *Chemical Geology* **266**, 187-193

1195 Valley J. W., Kitchen N., Kohn M. J., C.R. N. and Spicuzza M. J. (1995) UWG-2, a garnet
1196 standard for oxygen isotope ratios: strategies for high precision and accuracy with laser
1197 heating, *Geochimica et Cosmochimica Acta* **59**, 5223-5231
1198 Vallier T.L., Jenner G.A., Frey F.A., Gill, J.B., Davis A.S., Volpe A.M., Hawkins J.W., Morris
1199 J.D., Cawood P.A., Morton J.L., Scholl D.W., Rautenschlein M., White W.M., Williams
1200 R.W., Stevenson A.J. and White L.D. (1991) Subalkaline andesite from Valu Fa Ridge, a
1201 back-arc spreading center in southern Lau Basin: petrogenesis, comparative chemistry,
1202 and tectonic implications, *Chemical Geology* **91**, 227-256
1203 Van Keken P.E., Hacker B.R., Syracuse E.M. and Abers G.A. (2011) Subduction factory: 4.
1204 Depth-dependent flux of H_2O from subducting slabs worldwide, *Journal of Geophysical*
1205 *Research* **116**
1206 Varekamp J.C., Hesse A. and Mandeville C.W. (2010) Back-arc basalts from the Loncopue
1207 graben (Province of Neuquén, Argentina), *Journal of Volcanology and Geothermal*
1208 *Research* **197**, 313-328
1209 Vervoort J.D., Patchett P.J., Blichert-Toft J. and Albarède F. (1999)Relationships between Lu-Hf
1210 and Sm-Nd isotopic systems in the global sedimentary system, *Earth and Planetary*
1211 *Science Letters* **168**, 79-99
1212 Völker D., Reichel T., Wiedicke M. and Heubeck C. (2008) Turbidites deposited on Southern
1213 Central Chilean seamounts: Evidence for energetic turbidity currents, *Marine Geology*
1214 **251**, 15-31
1215 Völker D., Kutterolf S. and Wehrmann H. (2011) Comparative mass balance of volcanic edifices
1216 at the Southern Volcanic Zone of the Andes between 33°S and 46°S, *Journal of*
1217 *Volcanology and Geothermal Research* **205**, 114-129
1218 Wade J.A, Plank T., Stern R.J, Tollstrup D.L., Gill J.B., O'Leary J.C., Eiler J.M., Moore R.B.,
1219 Woodhead J.D., Trusdell F., Fisher T.P. and Hilton D.R. (2005) The May 2003 eruption of
1220 Anatahan volcano, Mariana Islands: Geochemical evolution of a silicic island-arc volcano,
1221 *Journal of Volcanology and Geothermal Research* **146**, 139-170
1222 Webb P.C., Thompson M., Potts P.J. and Enzweiler J. (2009) An international proficiency test
1223 for analytical geochemistry laboratories – report on round 25 (basalt, HTB-1), GeoPT25

1224 Woodhead J.D., Hergt J.M., Davidson J.P. and Eggins S.M. (2001) Hafnium isotope evidence
1225 for "conservative" element mobility during subduction zone processes, *Earth and*
1226 *Planetary Science Letters* **192**, 331-346
1227 Woodhead J.D., Stern R.J., Pearce J., Hergt J. and Vervoort J. (2012) Hf-Nd isotope variation in
1228 Mariana Trough basalts: The importance of "ambient mantle" in the interpretation of
1229 subduction zone magmas, *Geology* **40**, 539-542
1230 Workman R.K. and Hart S.R. (2005) Major and trace element composition of the depleted
1231 MORB mantle (DMM), *Earth and Planetary Science Letters* **231**, 53-42
1232 White W.M., Hofmann A.W. and Puchelt H. (1987) Isotope geochemistry of Pacific Mid-Ocean
1233 Ridge basalts, *Journal of Geophysical Research* **92**, 4881-4893
1234 Yododzinski G.M., Vervoort J.D., Brown S.T. and Gerseny M. (2010) Subduction controls Hf
1235 and Nd isotopes in lavas of the Aleutian island arc, *Earth and Planetary Science Letters*
1236 **300**, 226-238
1237 Yuan X., Ash G., Bataile K., Bohm M., Echtler H., Kind R., Oncken O. and Wölbern L. (2006)
1238 Deep seismic images of the Southern Andes, *Geological Society of America* special paper
1239 **407**, 61-72
1240 Zhang J-J, Zheng Y-F, and Zhao Z-F (2009) Geochemical evidence for interaction between
1241 oceanic crust and lithosphjeric mantle in the origin of Cenozoic continental basalts in east-
1242 central China. *Lithos* **110**, 305-326.
1243
1244 ***Table captions:***
1245
1246 **Table 1**. Major (wt. %) and trace elements (μg/g) for volcanic front, rear arc, backarc and
1247 sediment samples. Major element compositions recalculated to 100%, Total Fe expressed as
1248 FeO. N.d. = not determined. (+) No olivine observed on thin sections. (*) Original total retained.
1249
1250 **Table 2.** Sr-Nd-Hf-Pb-O isotopic compositions for volcanic front, rear arc, backarc and sediment
1251 samples. $\delta^{18}O_{melt}$ is calculated after Bindeman et al. (2004).
1252
1253 **Table 3.** Sediment (SED), altered oceanic crust (AOC) and depleted MORB Mantle (DMM)
1254 compositions used for the Arc Basalt Simulator 3 calculations. South Atlantic MORB – depleted

(SAM-D) – enriched (SAM-E). (*) See Table 4 for values used in calculation of the slab melt composition.

Table 4. Mixing and results parameters from the Arc Basalt Simulator 3. AOC = Altered Oceanic Crust, SED = Sediment.

Figure captions:

Figure 1. (a) Map of the Southern Volcanic Zone (SVZ) in Chile and Argentina between 30° and 45°S. Yellow triangles = Quaternary active volcanic front volcanoes. (b) Map of the Transitional Southern Volcanic Zone (TSVZ) between 34.5°S and 38°S. Red line = separates the Volcanic Arc (VA) and rear arc centers from the Backarc (BA). Blue circles and diamonds = northern and southern VA centers, respectively. Open circles = cinder cones from the Northern Backarc (NBA). Open circle with a cross = the Cerro Diamante stratovolcano that was an active arc center in the Miocene. Open triangles = central BA Pampas Negras volcanic field. Open = Southern Backarc (SBA; Auca Mahuida and Rio Colorado volcanic fields). Open crosses = Tromen stratovolcano area. Open cross with a dot = Buta Ranquil monogenetic center at the foot of Tromen. Yellow triangles = other Quaternary active VA volcanoes. Grey filled circles = major cities. Purple stars = the location of the SO210 cruise sediments. Red star = location of ODP site 1232. The white dashed lines bracket the TSVZ transect. The thick black line represents the border between Chile and Argentina. C.A. = Cerro Azul, L.M. = Laguna del Maule, I.V.F. = Infernillo Volcanic Field, R.C. = Rio Colorado, A.M. = Auca Mahuida. The ETOPO1 map source is from NOAA, modified (Amante and Eakins, 2009).

Figure 2. Total Alkali versus Silica [TAS] after Le Maitre et al. (1989). VA samples range from basalt to trachyandesite, BA samples are mostly alkali basalts and trachybasalts. BA samples are lower in silica than the VA samples except for one sample from Cerro Diamante stratovolcano.

Figure 3. MgO versus (a) FeOt, (b) CaO (c) Al_2O_3, (d) Na_2O, (e) TiO_2 and (f) P_2O_5. The VA and the BA generally form two different petrogenetic trends, reflecting different magma formation and evolution processes.

Figure 4. Multi-element diagram normalized to N-MORB after Sun and McDonough (1989), showing (a) the VA and trench sediments and (b) the BA. VA samples show typical subduction zone trace element signatures highlighted by Pb and K peaks and Nb and Ta troughs. More differentiated VA samples (with MgO < 5 wt. % and SiO_2 > 54 wt. %) show greater enrichment in Cs, Rb, Zr, and Hf, and depletion in Ti. BA samples from Pampas Negras and SBA show less pronounced peaks at Pb and K, and troughs at Nb and Ta, while NBA and Tromen samples have an intermediate subduction zone signature. Trench sediments from this study and Plank (2011) overlap the VA pattern.

Figure 5. $^{87}Sr/^{86}Sr$ versus $^{143}Nd/^{144}Nd$. VA and BA samples form two similar negative arrays which overlap almost completely. All samples from this study lie within the South Atlantic MORB field. The BA samples from the three segments (north, central = Pampas Negras, and south = SBA, Tromen) have distinct compositions (also see Figure 12). Trench sediments have similar Nd isotopes ratios as the volcanic rocks but more radiogenic Sr isotopes. The inset shows the TSVZ data (VA and BA) in a larger scale, including the Paleozoic metamorphic and intrusive basement in Chile and Argentina. VA literature data are from Hildreth and Moorbath (1988), Tormey et al. (1995), Davidson et al. (1987, 1988), Hickey-Vargas et al. (1986), Harmon et al. (1984), and Sigmarsson et al. (1990). BA literature data are from Kay et al. (2006a,b,c) and Varekamp et al. (2010). Trench sediment data are from this study and Lucassen et al. (2010). Basement data are from Lucassen et al. (2004). East Pacific Rise (20-34°S) MORB data are from Fontignie and Schilling (1991), Haase (2002), Hamelin et al. (1984), Hanan and Schilling (1989), Ito et al. (1980), Ito et al. (1987), Kingsley et al. (2007), MacDougall et al. (1986), Mahoney et al. (1993), Newsom et al. (1986) and White et al. (1987). South Atlantic (30-50°S) MORB data are from Andres et al. (2002), Douglas et al. (1999), Fontignie and Schilling (1996), Hanan et al. (1986) and Roy-Barman et al. (1998).

Figure 6. $^{206}Pb/^{204}Pb$ versus (a) $^{207}Pb/^{204}Pb$, (b) $^{208}Pb/^{204}Pb$ and (c) $\delta^{18}O_{olivine}$. The samples form positive arrays from the BA to the VA with good correlations represented by the thin black lines (r^2 = 0.941 and 0.968 if the Buta Ranquil sample is excluded). An extrapolation of the arrays intersects the South Atlantic MORB but not the East Pacific Rise MORB field. The trench

sediments fall at the radiogenic end of the BA-VA arrays. The Cretaceous to Paleozoic basement fields overlap the data on the thorogenic Pb isotope diagram but have higher $^{207}Pb/^{204}Pb$ on the uranogenic Pb isotope diagram. The NBA samples are shifted to lower $^{207}Pb/^{204}Pb$ or more Pacific MORB-like compositions compared to the VA samples. There is no correlation between O isotopes and Pb isotopes. Data sources are the same as in Figure 5. Trench sediment field includes river mouth sediments from Hildreth and Moorbath (1988).

Figure 7. $^{206}Pb/^{204}Pb$ (a) versus Ce/Pb, (b) Nb/U, and (c) Nb/Zr. The data form good negative correlations for the BA to the VA data (r^2 = 0.809, 0.841 and 0.704, respectively). Two-component mixing must form a straight line when the denominator is the same on both axis as in (a). The VA samples overlap the trench sediment field. The SBA samples extend to higher Ce/Pb, Nb/U and Nb/Zr than the Pampas Negras basalts which have similar Pb isotope ratios, which we believe reflects source heterogeneity. MORB field is represented by the dashed line box (range in average values for MORB and OIB from Hoffman et al., 1986). Trench sediments are from this study and Lucassen et al. (2010). AOC is from Tollstrup et al. (2010)

Figure 8. εNd versus εHf. The VA and BA samples form separate subparallel positive correlations with correlation coefficients (r^2) of 0.87 and 0.79, respectively. VA samples have higher εHf than the BA for a given εNd. The thick black line represents the mantle array (Geldmacher et al., 2006). Data sources are the same as in Figure 5. The Peru/Chile trench sediments are from Vervoort et al. (1999) and Vervoort et al. (2011).

Figure 9. SiO_2 versus (a) Ce/Pb, (b) Nb/Zr, (c) $^{87}Sr/^{86}Sr$, (d) $^{143}Nd/^{144}Nd$, (e) $^{207}Pb/^{204}Pb$ and (f) $\delta^{18}O_{olivine}$. There is no clear correlation for the VA or BA samples between SiO_2 and isotopes or trace element ratios used in this paper indicating that assimilation of old sialic crust during differentiation does not significantly modify these isotopes and trace element ratios in our samples.

Figure 10. Nb/U versus Ce/Pb. The VA and BA samples form an array from the trench sediments field to the MORB-OIB mantle field represented by the dashed line box (range in average values for MORB and OIB from Hoffman et al., 1986). The correlation (r^2 = 0.925)

indicates the presence of variable amounts of a uniform slab component in all samples, but least at the SBA and Pampas Negras. Trench sediments are from this study and Lucassen et al. (2010). AOC is from Tollstrup et al. (2010)

Figure 11. Nb/Yb versus Th/Yb, after Pearce (2008). MORB and OIB define the positive trend labeled MORB-OIB array, reflecting greater mantle enrichment at higher ratios. VA and NBA samples lie above this array due to the addition of a Th-bearing slab component whereas most BA samples from Pampas Negras and the SBA lie within the mantle array or straddle its boundary and therefore lack slab-derived Th. The VA samples overlap, but show a larger range, than the trench sediments (grey field). Data sources are the same as in Figure 10.

Figure 12. (a) $^{87}Sr/^{86}Sr$ versus $^{143}Nd/^{144}Nd$ and (b) $^{206}Pb/^{204}Pb$. The mixing lines are from the Arc Basalt Simulator 3.10 models for the VA. The dashed line represents mixing between altered oceanic crust (AOC) and sediment (SED). The thin lines represent mixing between a melt of a 60:40 SED:AOC source with South Atlantic MORB, and depleted (SAM-D) or enriched (SAM-E) mantle (the two stars). The labeled tick marks show the amount of slab component added to the mantle. Source compositions are in Table 3. Slab and mantle melting conditions are described in the text and summarized in Table 4. For partition coefficients and melting modes for the slab and mantle see Kimura et al. (2010). AOC is from Tollstrup et al. (2010).

Figure 13. $\delta^{18}O_{olivine}$ versus $^{87}Sr/^{86}Sr$. The mixing lines are from the Arc Basalt Simulator 3.10 models for the VA. The thin line represents the mixing between a slab component of 60:40 SED:AOC source on one hand and depleted (SAM-D) mantle (stars) on the other. The labeled tick marks show the amount of slab component added to the mantle. Source compositions are in Table 3. The isotope ratios of the slab component (60% SED and 40% AOC) are calculated from the data in Table 3.

Table 1

Sample number	Sample Location	Country	Sample type	Lat (S)	Long (W)	Distance from VF (Km)	Group
Volcanic Front							
CL 721D	Tinguiririca	Chile	lava	-34.8253	-70.3699	0	VA
CL 725	Tinguiririca	Chile	lava	-34.8253	-70.3699	0	VA
CL 726(+)	Tinguiririca	Chile	lava	-34.8253	-70.3699	0	VA
CL 207	Planchón-Peteroa	Chile	lava	-35.2126	-70.5251	0	VA
CL 736	Resolana (small cone near Cerro Azul)	Chile	lava	-35.6708	-70.8364	0	VA
CL 741	Resolana	Chile	bomb	-35.6566	-70.8379	0	VA
CL 745	Resolana	Chile	bomb	-35.6392	-70.8351	0	VA
CL 196	Los Hornitos (small cone near Cerro Azul)	Chile	tephra	-35.7266	-70.7861	0	VA
CL 565(+)	San Pedro	Chile	lava	-36.0122	-70.8371	0	VA
CL 568	San Pedro	Chile	lava	-36.0114	-70.8330	0	VA
CL 570	San Pedro	Chile	lava	-36.0133	-70.8218	0	VA
CL 571	San Pedro	Chile	lava	-36.0182	-70.8121	0	VA
CL 572	San Pedro (Satellite cones)	Chile	bomb	-36.1025	-70.6995	0	VA
CL 575b	San Pedro (Satellite cones)	Chile	bomb	-36.0858	-70.6954	0	VA
CL 576	San Pedro (Satellite cones)	Chile	lava	-36.1025	-70.6995	0	VA
CL 577	San Pedro (Satellite cones)	Chile	lava	-36.0993	-70.7033	0	VA
CL 447(+)	Longaví	Chile	lava	-36.1231	-71.2228	0	VA
CL 449	Longaví	Chile	lava	-36.1735	-71.1661	0	VA
CL 520	Longaví	Chile	lava	-36.1735	-71.1661	0	VA
CL 530	Longaví	Chile	lava	-36.1849	-71.1609	0	VA
CL 531	Longaví	Chile	lava	-36.1896	-71.1615	0	VA
CL 555	Paranor (Chillán Satellite cone)	Chile	bomb	-36.8767	-71.4291	0	VA
CL 071	Antuco	Chile	lava	-37.3971	-71.4321	0	VA
CL 080	Antuco	Chile	tephra	-37.4132	-71.2924	0	VA
CL 085	Antuco	Chile	lava	-37.3711	-71.3524	0	VA
CL 557	Callaqui (Satellite cones)	Chile	lava	-37.9077	-71.3989	0	VA
CL 559	Callaqui (Satellite cones)	Chile	lava	-37.9090	-71.3951	0	VA
CL 560	Callaqui (Satellite cones)	Chile	lava	-37.9090	-71.3951	0	VA
Rear arc							
CL 323	Laguna de la Ninna Encantada	Argentina	lava	-35.1623	-69.8716	70	VA
CL 325	Infernillo	Argentina	lava	-35.1750	-69.7960	70	VA
CL 220	Laguna del Maule	Chile	lava	-35.9971	-70.5613	20	VA
CL 221	Laguna del Maule	Chile	lava	-35.9694	-70.5687	20	VA
CL 563	Copahue	Chile	bomb	-37.8604	-71.1635	20	VA
Backarc							
CL 273	Cerro Chato	Argentina	lava	-34.4780	-68.8423	140	Northern Backarc
CL 274	Cerro Chato	Argentina	lava	-34.4718	-68.8730	140	Northern Backarc
CL 279	Cerro Diamante	Argentina	lava	-34.6328	-69.0891	130	Northern Backarc
CL 277	Cerro Diamante	Argentina	lava	-34.5919	-69.0351	130	Northern Backarc
CL 304	Diamante Chico	Argentina	lava	-34.6598	-69.0322	130	Northern Backarc
CL 308	Trintrica	Argentina	lava	-35.3737	-68.7379	190	Northern Backarc
CL 313	Llancanelo field	Argentina	lava	-35.2906	-68.2378	240	Northern Backarc
CL 318	Cones South-East of El Nihuil	Argentina	lava	-35.3255	-68.3877	225	Northern Backarc
CL 346	Cerro Malacara	Argentina	lava	-35.7102	-69.4606	120	Northern Backarc
CL 350	Eastern Cerro Malacara	Argentina	lava	-35.7922	-69.4632	120	Northern Backarc
CL 354	Cerro los Leones	Argentina	bomb	-35.4960	-69.4504	120	Northern Backarc
CL 360	Pampas Negras	Argentina	lava	-36.2892	-69.5751	150	Pampas Negras
CL 367	Pampas Negras	Argentina	lava	-36.3372	-69.4705	150	Pampas Negras
CL 371	Pampas Negras	Argentina	lava	-36.3745	-69.4016	150	Pampas Negras
CL 372	Pampas Negras	Argentina	lava	-36.3748	-69.4025	150	Pampas Negras
CL 387	Pampas Negras	Argentina	bomb	-36.3190	-69.6836	145	Pampas Negras
CL 472	Buta Ranquil	Argentina	bomb	-37.0071	-69.8230	140	Buta Ranquil
CL 406	Tromen	Argentina	bomb	-37.0342	-69.8503	140	Tromen area
CL 410	Tromen	Argentina	lava	-36.9889	-69.9988	140	Tromen area
CL 411	Tromen	Argentina	lava	-37.0671	-70.0638	140	Tromen area
CL 412	Tromen	Argentina	lava	-36.9935	-70.0100	140	Tromen area
CL 392	Auca Mahuida	Argentina	bomb	-37.7206	-68.9232	245	Southern Backarc
CL 394	Auca Mahuida	Argentina	lava	-37.7271	-68.8905	245	Southern Backarc
CL 401	Auca Mahuida	Argentina	bomb	-37.6061	-68.8147	245	Southern Backarc
CL 404	Auca Mahuida	Argentina	bomb	-37.3019	-68.9069	245	Southern Backarc
CL 456	Cerro Redondo, Rio Colorado	Argentina	bomb	-37.3019	-68.9069	280	Southern Backarc
CL 459	Cerro Mendez, Rio Colorado	Argentina	bomb	-37.3401	-68.9641	280	Southern Backarc
Sediments							
SO210-#01_T	Incoming Plate	Chile	Trench sediment	-33.1995	-73.5713		
SO210-#01_B	Incoming Plate	Chile	Trench sediment	-33.1995	-73.5713		
SO210-#05_T	Incoming Plate	Chile	Trench sediment	-35.1667	-74.6666		
SO210-#05_B	Incoming Plate	Chile	Trench sediment	-35.1667	-74.6666		
SO210-#13_T	Incoming Plate	Chile	Trench sediment	-36.5000	-75.1665		
SO210-#13_B	Incoming Plate	Chile	Trench sediment	-36.5000	-75.1665		
SO210-#12_T	Incoming Plate	Chile	Trench sediment	-35.8334	-74.7051		
SO210-#12_B	Incoming Plate	Chile	Trench sediment	-35.8334	-74.7051		
SO210-#43_T	BioBio Slide	Chile	Trench sediment	-36.6341	-73.7627		
SO210-#43_B	BioBio Slide	Chile	Trench sediment	-36.6341	-73.7627		
Reference materials							
BHVO							

Table 2

Sample number Volcanic Front	Sample Location	$^{87}Sr/^{86}Sr$	2σ	$^{143}Nd/^{144}Nd$	2σ	εNd	$^{176}Hf/^{177}Hf$	2σ	εHf	$^{206}Pb/^{204}Pb$
CL 721D	Tinguiririca	0.703909	0.000003	0.512752	0.000002	2.22				18.6383
CL 725	Tinguiririca	0.704139	0.000002	0.512751	0.000003	2.21	0.282926	0.000005	5.44	18.6493
CL 726	Tinguiririca	0.703970	0.000003	0.512745	0.000002	2.08	0.282928	0.000005	5.52	18.6375
CL 207	Planchón-Peteroa	0.704108	0.000003	0.512752	0.000005	2.22	0.282978	0.000004	7.27	18.5813
CL 736	Resolana (small cone near Cerro Azul)	0.703769	0.000003	0.512795	0.000002	3.07				18.6028
CL 741	Resolana	0.703645	0.000003	0.512833	0.000003	3.81	0.283004	0.000004	8.19	18.6020
CL 745	Resolana	0.703747	0.000003	0.512803	0.000002	3.22	0.282979	0.000003	7.33	18.6057
CL 196	Los Hornitos (small cone near Cerro Azul)	0.703738	0.000003	0.512828	0.000003	3.70	0.283026	0.000005	8.99	18.6291
CL 196_rep							*0.283015*	*0.000004*	*8.60*	
CL 565	San Pedro	0.703928	0.000003	0.512799	0.000003	3.15				18.5707
CL 568	San Pedro	0.704016	0.000003	0.512788	0.000003	2.92	0.282970	0.000006	7.01	18.6074
CL 570	San Pedro	0.704065	0.000003	0.512767	0.000003	2.51				18.5922
CL 571	San Pedro	0.704023	0.000003	0.512785	0.000003	2.86	0.282981	0.000006	7.39	18.6042
CL 571_rep		*0.704009*	*0.000003*	*0.512780*	*0.000002*	*2.76*				*18.6064*
CL 572	San Pedro (Satellite cones)	0.704050	0.000003	0.512752	0.000003	2.23				18.6093
CL 575b	San Pedro (Satellite cones)	0.704046	0.000003	0.512749	0.000003	2.17	0.282943	0.000006	6.06	18.6123
CL 576	San Pedro (Satellite cones)	0.704053	0.000003	0.512756	0.000003	2.30				18.6135
CL 577	San Pedro (Satellite cones)	0.704161	0.000003	0.512714	0.000002	1.48				18.6205
CL 447	Longaví	0.703803	0.000003	0.512869	0.000002	4.51				18.5561
CL 449	Longaví	0.704105	0.000003	0.512761	0.000003	2.40	0.282964	0.000006	6.79	18.6444
CL 520	Longaví	0.703903	0.000003	0.512844	0.000003	4.02				18.5762
CL 530	Longaví	0.704029	0.000003	0.512798	0.000003	3.12	0.282994	0.000005	7.83	18.5860
CL 531	Longaví	0.703979	0.000003	0.512806	0.000003	3.27				18.5868
CL 555	Paranor (Chillán Satellite cone)	0.703915	0.000003	0.512836	0.000003	3.87				18.5981
CL 071	Antuco	0.703853	0.000003	0.512839	0.000003	3.91	0.283020	0.000005	8.78	18.5824
CL 080	Antuco	0.703863	0.000003	0.512835	0.000002	3.85				18.5724
CL 085	Antuco	0.703840	0.000003	0.512847	0.000002	4.07				18.5836
CL 557	Callaqui (Satellite cones)	0.703939	0.000003	0.512814	0.000003	3.44				18.5866
CL 559	Callaqui (Satellite cones)	0.703854	0.000002	0.512807	0.000003	3.30	0.283011	0.000006	8.46	18.5687
CL 560	Callaqui (Satellite cones)	0.703907	0.000003	0.512814	0.000003	3.43				18.6306
CL 560_rep		*0.703853*	*0.000003*	*0.512807*	*0.000002*	*3.30*				*18.6339*
Rear arc										
CL 323	Laguna de la Ninna Encantada	0.704150	0.000003							18.6744
CL 325	Infernillo	0.704228	0.000003	0.512708	0.000003	1.36				18.6870
CL 220	Laguna del Maule	0.704059	0.000003	0.512760	0.000003	2.39				18.6241
CL 221	Laguna del Maule	0.704074	0.000003	0.512756	0.000003	2.29	0.282954	0.000007	6.44	18.6251
CL 563	Copahue	0.703922	0.000002	0.512780	0.000003	2.77				18.5887
Backarc										
CL 273	Cerro Chato	0.703971	0.000004	0.512816	0.000002	3.48				18.5626
CL 274	Cerro Chato	0.704129	0.000003	0.512767	0.000002	2.51				18.6066
CL 279	Cerro Diamante	0.704246	0.000003	0.512705	0.000002	1.30				18.4662
CL 277	Cerro Diamante	0.704125	0.000003	0.512766	0.000002	2.50	0.282884	0.000006	3.95	18.5171
CL 304	Diamante Chico	0.704213	0.000002	0.512764	0.000002	2.46				18.5908
CL 308	Trintrica	0.703908	0.000003	0.512822	0.000002	3.59				18.5405
CL 313	Llancanelo field	0.704040	0.000003	0.512781	0.000002	2.78	0.282894	0.000005	4.32	18.5136
CL 318	Cones South-East of El Nihuil	0.704029	0.000003	0.512792	0.000003	3.00				18.5191
CL 346	Cerro Malacara	0.704074	0.000003	0.512769	0.000003	2.56				18.4954
CL 350	Eastern Cerro Malacara	0.704114	0.000003	0.512737	0.000003	1.92				18.4589
CL 354	Cerro los Leones	0.704009	0.000003	0.512769	0.000003	2.56				18.4737
CL 360	Pampas Negras	0.703904	0.000003	0.512793	0.000003	3.03	0.282901	0.000005	4.58	18.3755
CL 367	Pampas Negras	0.703890	0.000003	0.512791	0.000003	2.98	0.282915	0.000006	5.05	18.2966
CL 367_rep		*0.703902*	*0.000003*	*0.512788*	*0.000002*	*2.93*				*18.2955*
CL 371	Pampas Negras	0.703946	0.000003	0.512768	0.000003	2.53				18.3264
CL 372	Pampas Negras	0.703915	0.000003	0.512789	0.000003	2.95	0.282894	0.000006	4.33	18.3326
CL 387	Pampas Negras	0.703999	0.000003	0.512772	0.000002	2.61				18.4152
CL 472	Buta Ranquil	0.704065	0.000003	0.512877	0.000003	4.66	0.283003	0.000006	8.17	18.5278
CL 412_rep		*0.704038*	*0.000003*	*0.512890*	*0.000003*	*4.91*				18.5281
CL 406	Tromen	0.703851	0.000003	0.512833	0.000003	3.81				18.5299
CL 410	Tromen	0.704096	0.000003	0.512761	0.000003	2.40				18.5656
CL 411	Tromen	0.703927	0.000003	0.512791	0.000003	2.98				18.5455
CL 412	Tromen	0.704329	0.000003	0.512725	0.000002	1.69				18.5791
CL 392	Auca Mahuida	0.703777	0.000003	0.512809	0.000002	3.34				18.4113
CL 394	Auca Mahuida	0.703727	0.000003	0.512823	0.000002	3.61				18.3893
CL 401	Auca Mahuida	0.703749	0.000003	0.512805	0.000002	3.25				18.3959
CL 404	Auca Mahuida	0.703881	0.000003	0.512804	0.000003	3.25				18.4568
CL 456	Cerro Redondo, Rio Colorado	0.703641	0.000002	0.512840	0.000002	3.94	0.282914	0.000004	5.02	18.3811
CL 456_rep		*0.703620*	*0.000003*	*0.512846*	*0.000003*	*4.05*				*18.3809*
CL 459	Cerro Mendez, Rio Colorado	0.703598	0.000003	0.512857	0.000002	4.27	0.282941	0.000004	5.97	18.3620
Sediments										
SO210-#01_T	Incoming Plate									
SO210-#01_B	Incoming Plate	0.705984	0.000003	0.512690	0.000003	1.01	0.282990	0.000004	7.72	18.6116
SO210-#05_T	Incoming Plate									
SO210-#05_B	Incoming Plate	0.705623	0.000003	0.512699	0.000003	1.19	0.282982	0.000005	7.41	18.6252
SO210-#13_T	Incoming Plate									
SO210-#13_B	Incoming Plate	0.705889	0.000003	0.512701	0.000002	1.22	0.282980	0.000005	7.36	18.6291
SO210-#12_T	Incoming Plate									
SO210-#12_B	Incoming Plate	0.705605	0.000003	0.512700	0.000001	1.21				18.6310
SO210-#43_T	BioBio Slide									
SO210-#43_B	BioBio Slide	0.704163	0.000003	0.512815	0.000001	3.45	0.283015	0.000003	8.48	18.5776

Table 3

	AOC	SED	Slab melt	SAM-D	SAM-E
			60SED:40AOC(*)	*DMM*	*E-DMM*
Rb	13.7	44.7	16.7	0.050	0.108
Ba	15.6	1238	1286	0.563	1.22
Th	0.173	5.70	5.64	0.008	0.016
U	0.390	3.21	3.48	0.003	0.005
Nb	2.89	4.63	1.01	0.149	0.246
Ta	0.210	0.350	0.081	0.010	0.016
K	5147	17483	6476	80.0	120
La	3.40	13.5	11.0	0.192	0.253
Ce	11.4	32.4	31.7	0.550	0.726
Pb	0.437	17.5	18.7	0.018	0.024
Pr	2.06	3.93	4.15	0.107	0.132
Sr	109	257	311	7.66	9.72
Nd	11.3	16.3	16.8	0.581	0.703
Sm	3.95	3.65	2.72	0.239	0.273
Zr	112	123	84.4	5.08	6.09
Hf	3.00	3.40	2.36	0.157	0.186
Eu	1.34	0.905	0.614	0.096	0.108
Gd	5.55	3.51	1.58	0.358	0.397
Tb	1.01	0.547	0.164	0.070	0.076
Dy	6.56	3.32	0.750	0.505	0.543
Y	40.7	18.1	3.15	2.66	3.55
Ho	1.43	0.674	0.112	0.115	0.123
Er	4.09	1.88	0.290	0.348	0.369
Tm	4.02	0.290	0.141	0.055	0.055
Yb	0.636	1.97	0.110	0.365	0.382
Lu	3.07	0.298	0.081	0.058	0.060
$^{87}Sr/^{86}Sr$	0.704769	0.705637	0.705480	0.703300	0.704200
$^{143}Nd/^{144}Nd$	0.513153	0.512673	0.512946	0.512940	0.512690
$^{206}Pb/^{204}Pb$	18.54	18.71	18.71	18.15	18.25
$^{207}Pb/^{204}Pb$	15.45	15.63	15.63	15.54	15.55
$^{208}Pb/^{204}Pb$	37.70	38.65	38.64	38.00	38.10
$\delta^{18}O$ (‰)	2	9	6.2	5.25	5.25

Table 4

			Sr	Nd
Slab	P (Gpa)	4		
	T (°C)	827		
AOC	Melting (%)	18		
	Xgar	45.8		
	Xcpx	42.8		
	Xphen	1.04		
	Xrut	1.28		
	Bulk D		0.034	0.404
SED	Melting (%)	18		
	Xgar	24.7		
	Xcpx	15.8		
	Xphen	28.9		
	Xrut	0.80		
	Bulk D		0.404	1.63
Mantle	P (Gpa)	2.1		
	T (°C)	1270		
	Slab component added (%)	0.5-1		
	Mantle melting (%)	1-1.2		
	Bulk D		0.022	0.028

Figure 1

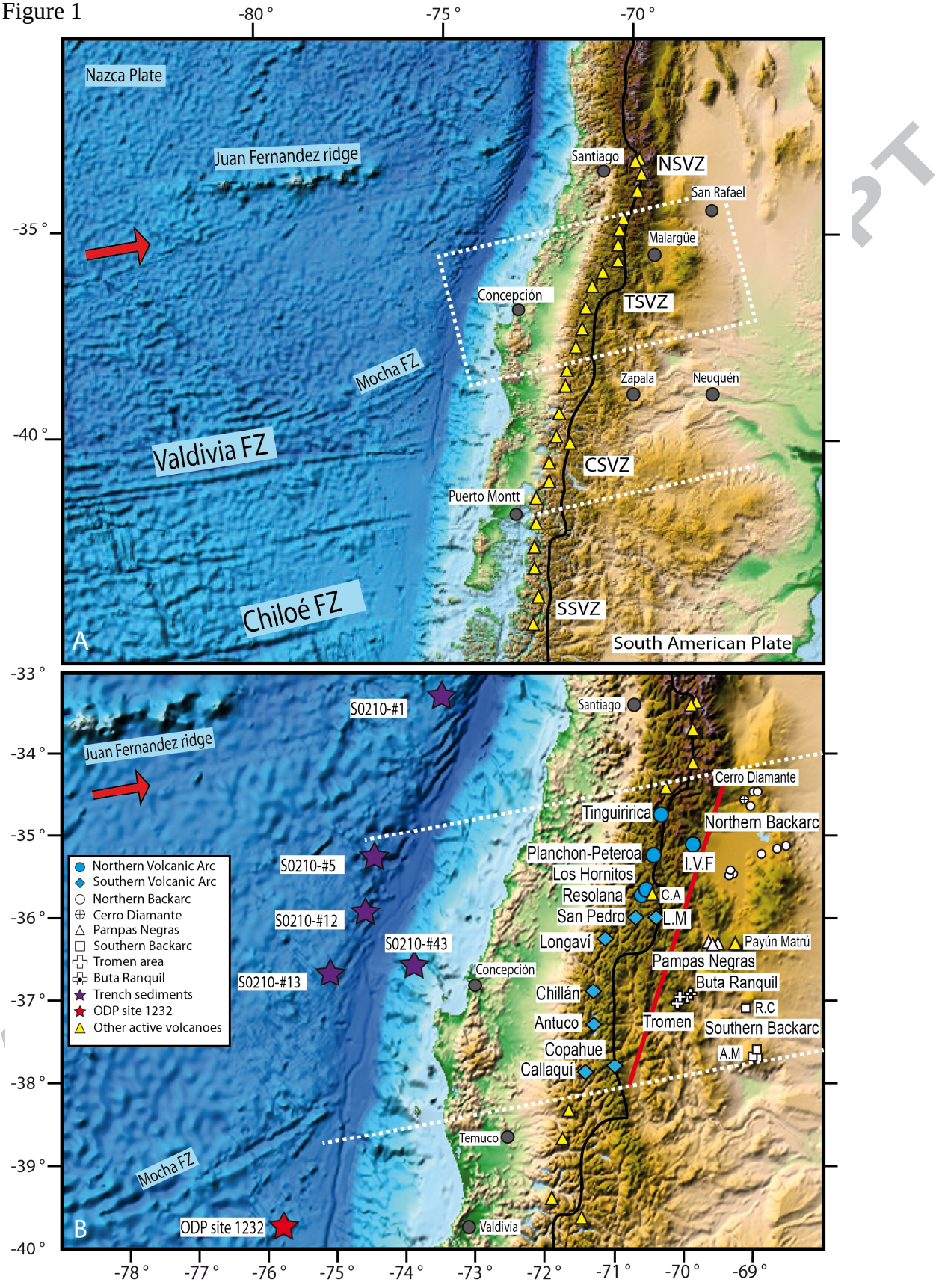

Figure 2

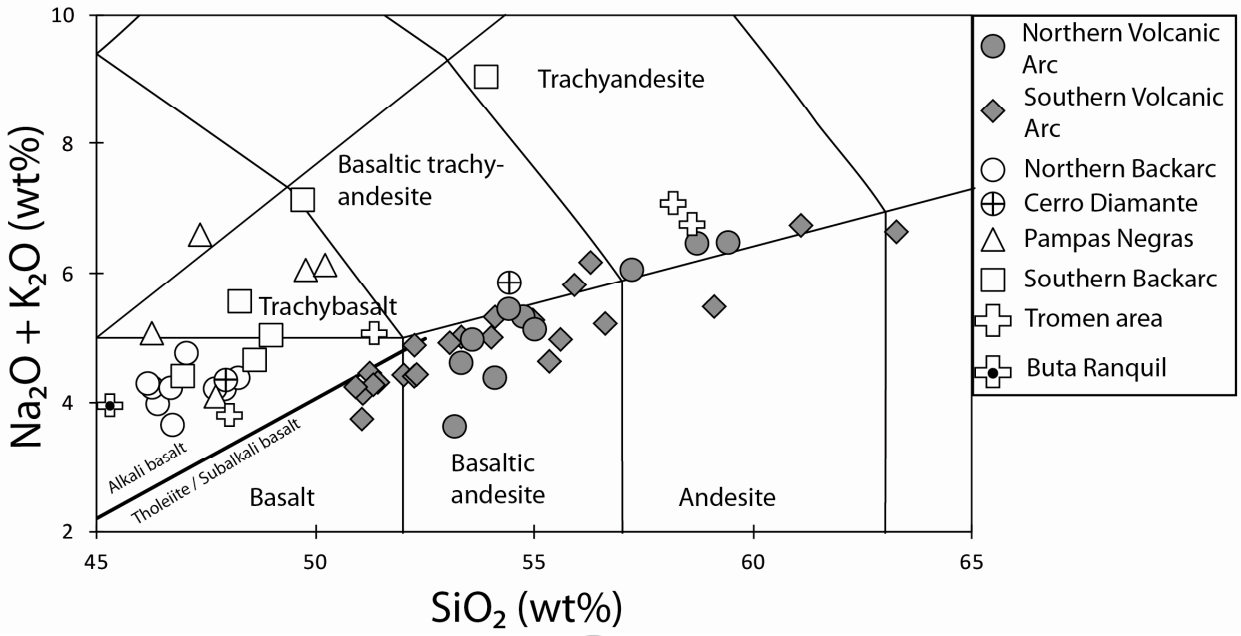

Figure 3

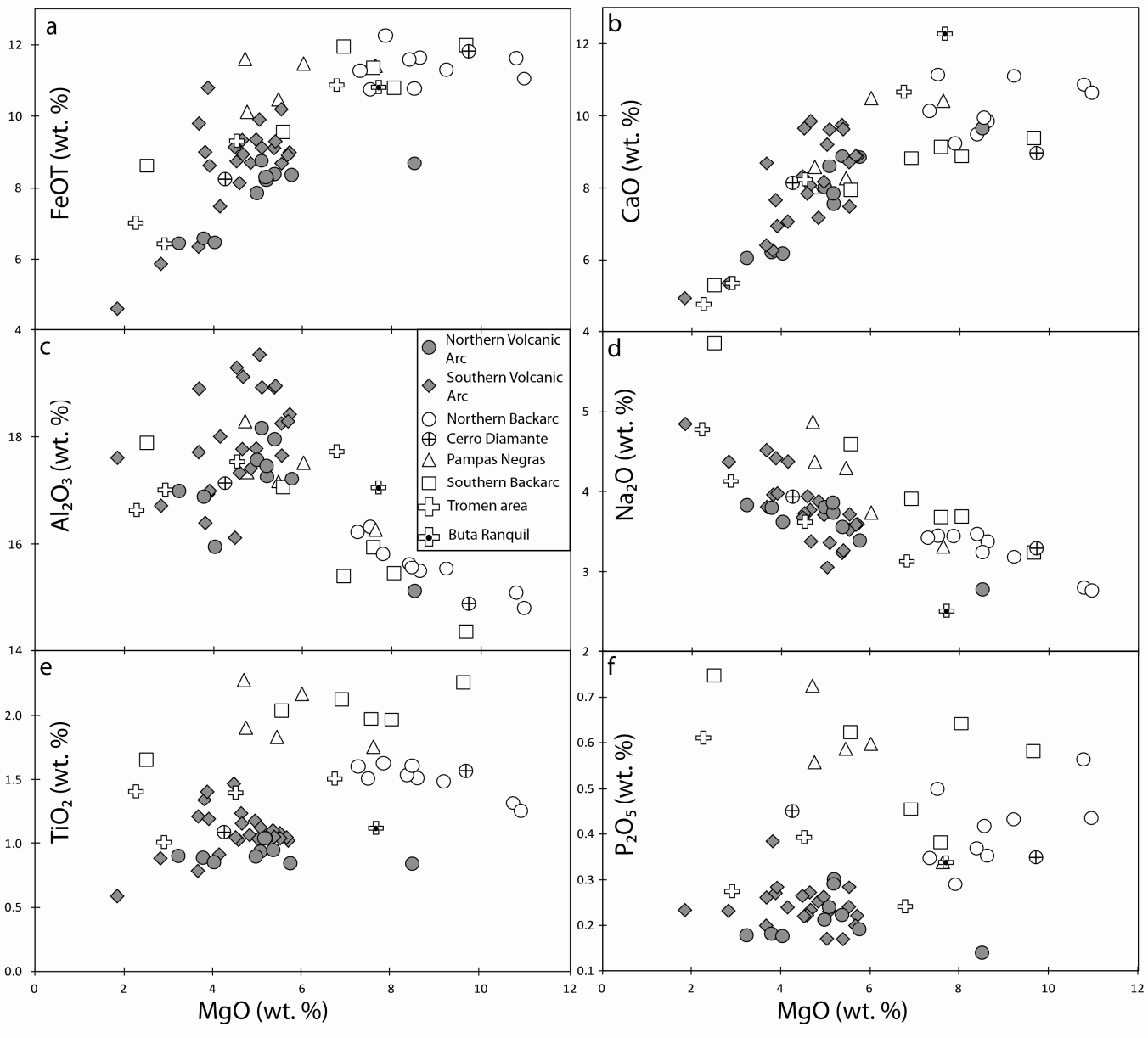

Figure 4

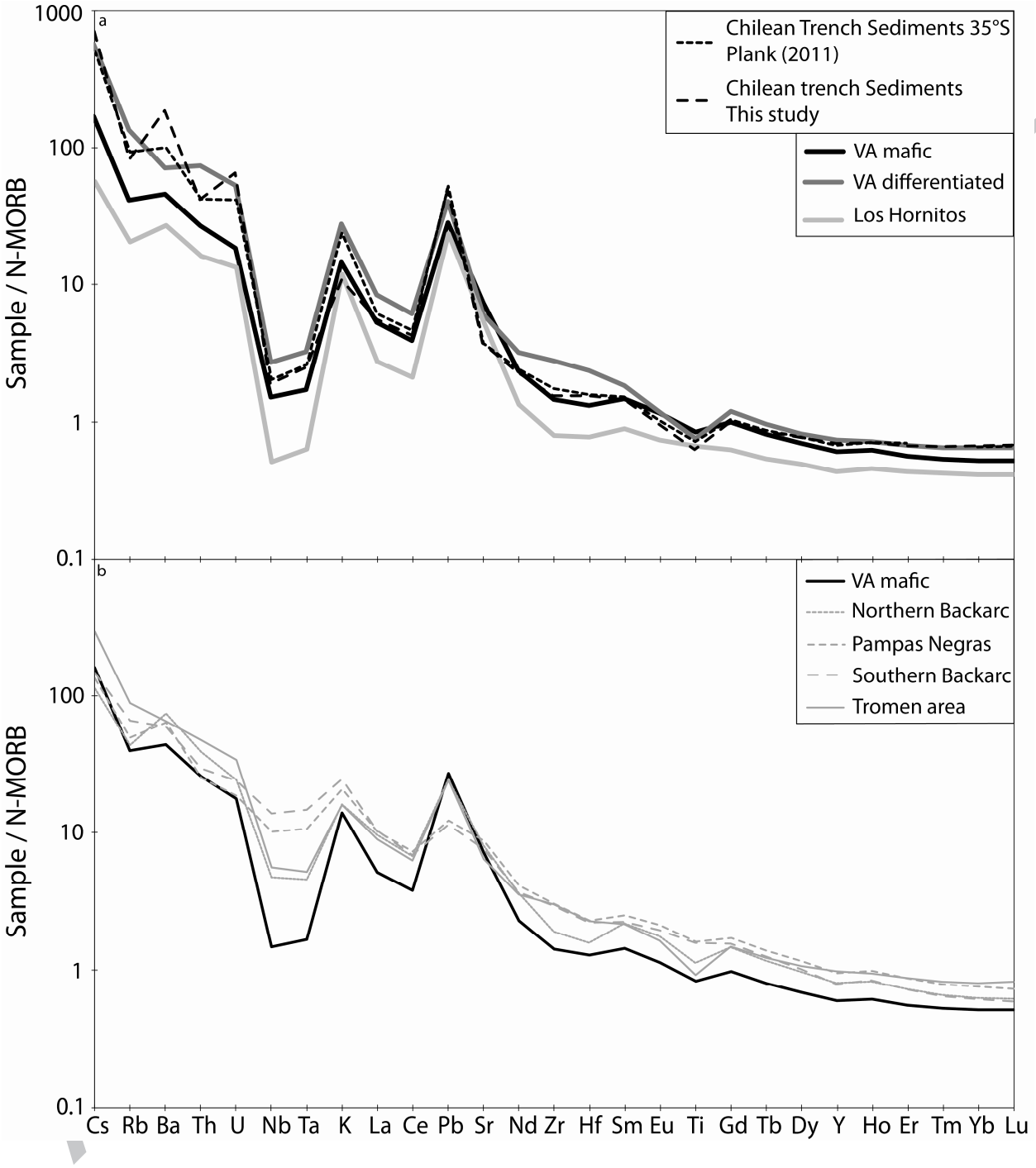

Figure 5

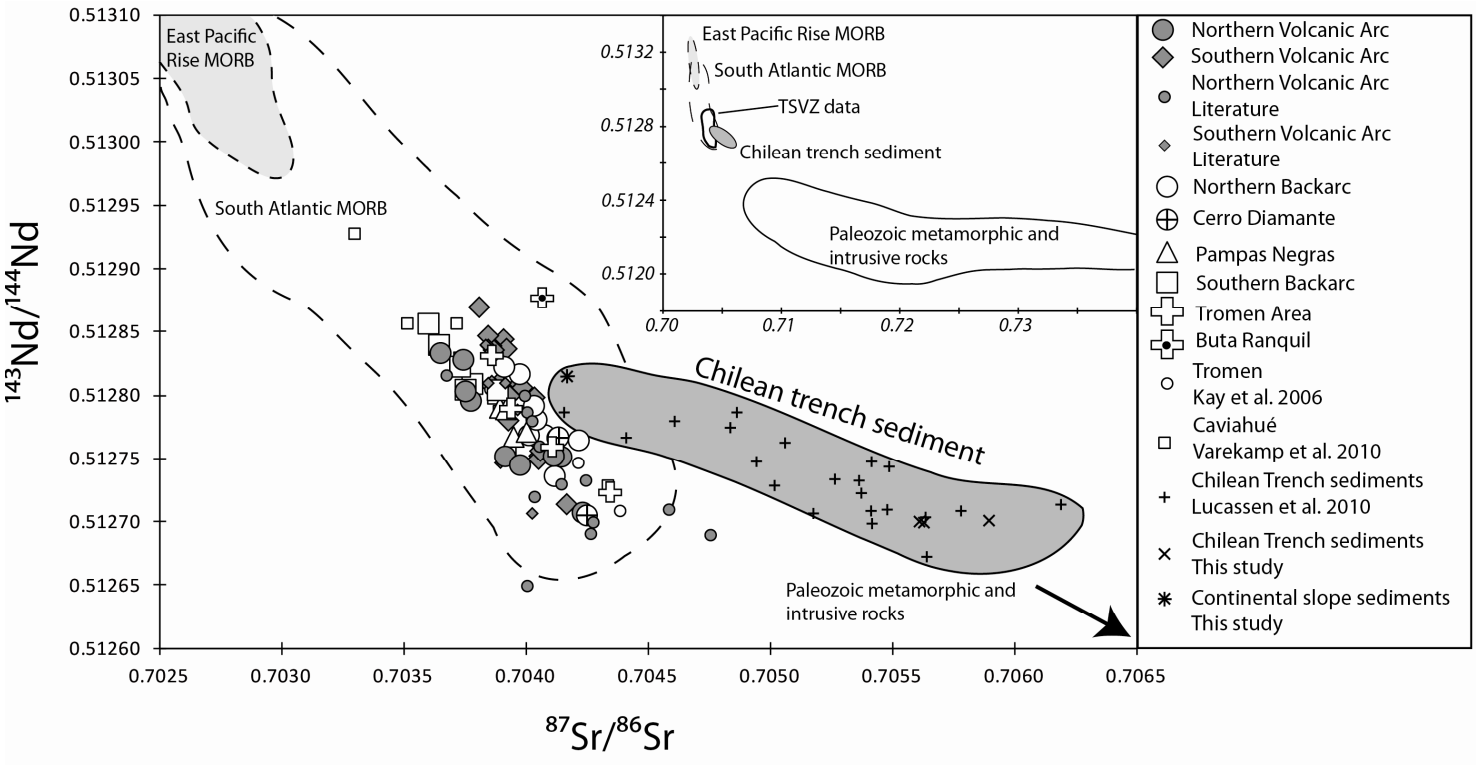

Figure 6

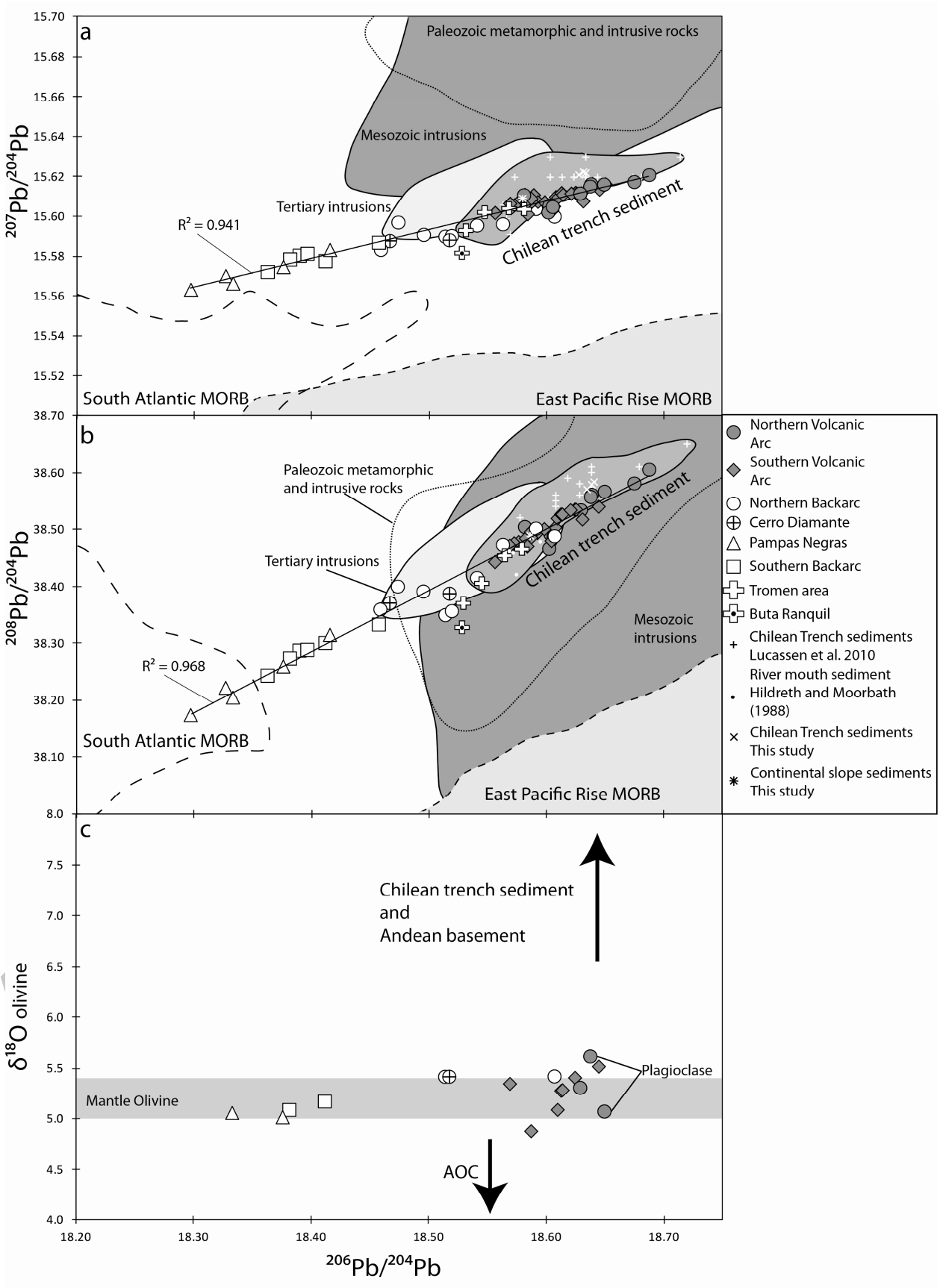

Figure 7

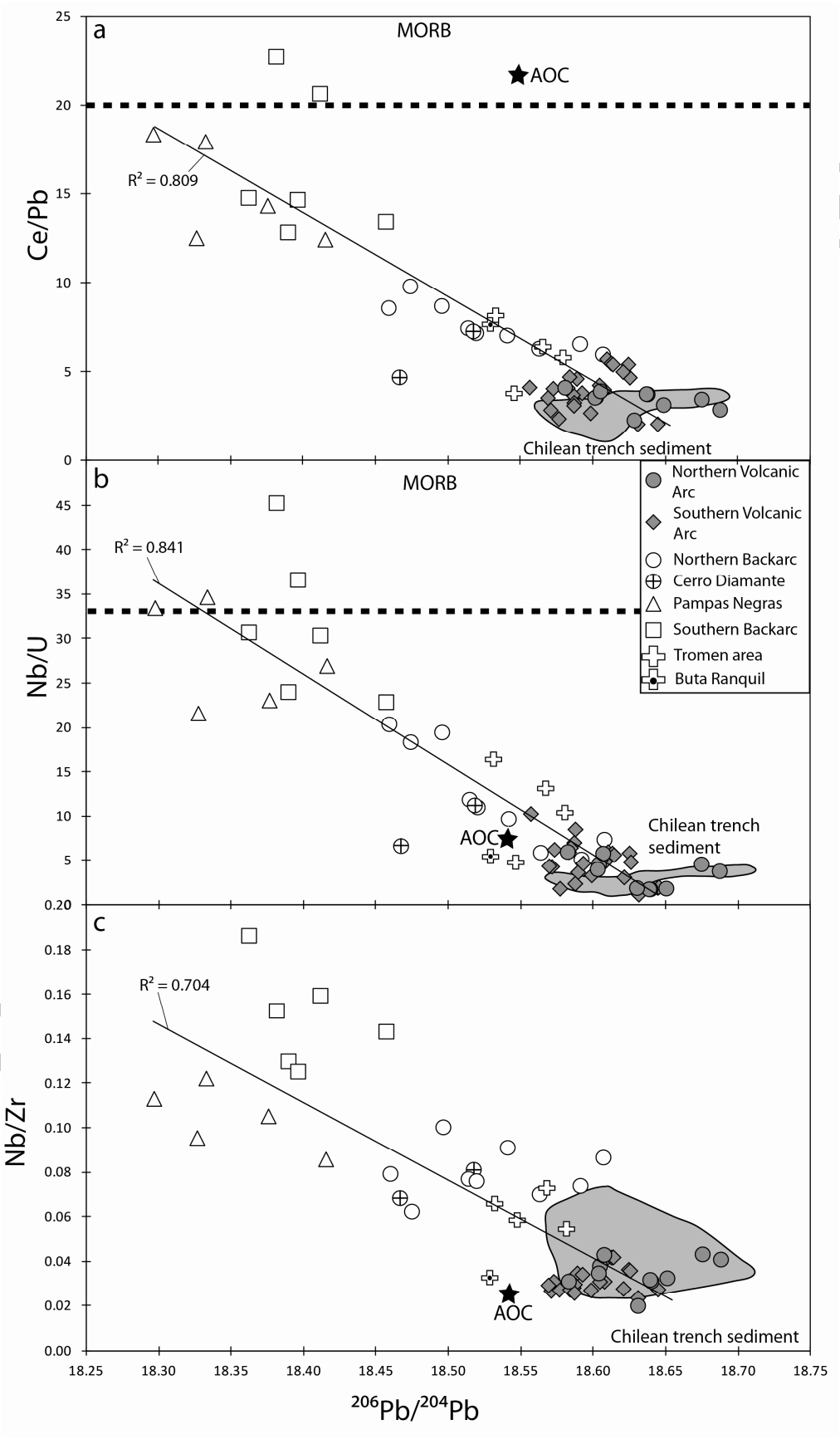

Figure 8

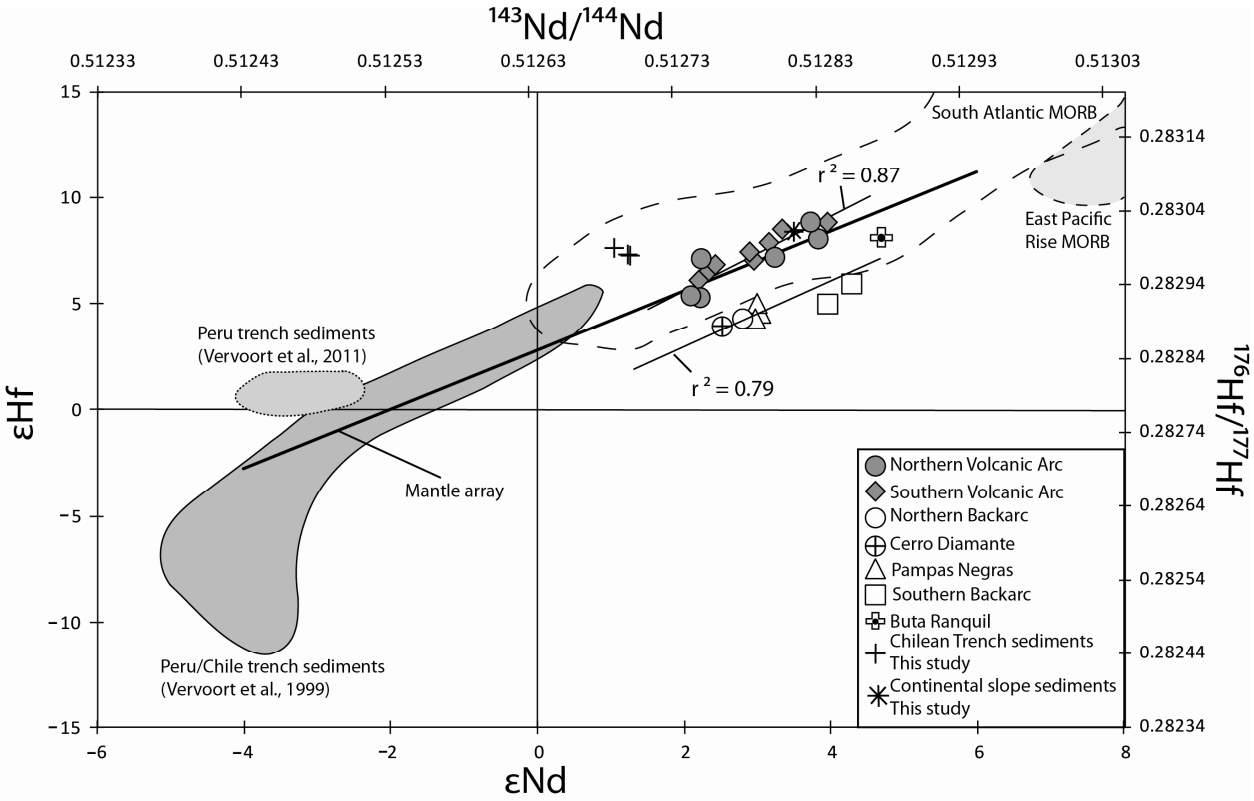

Figure 9

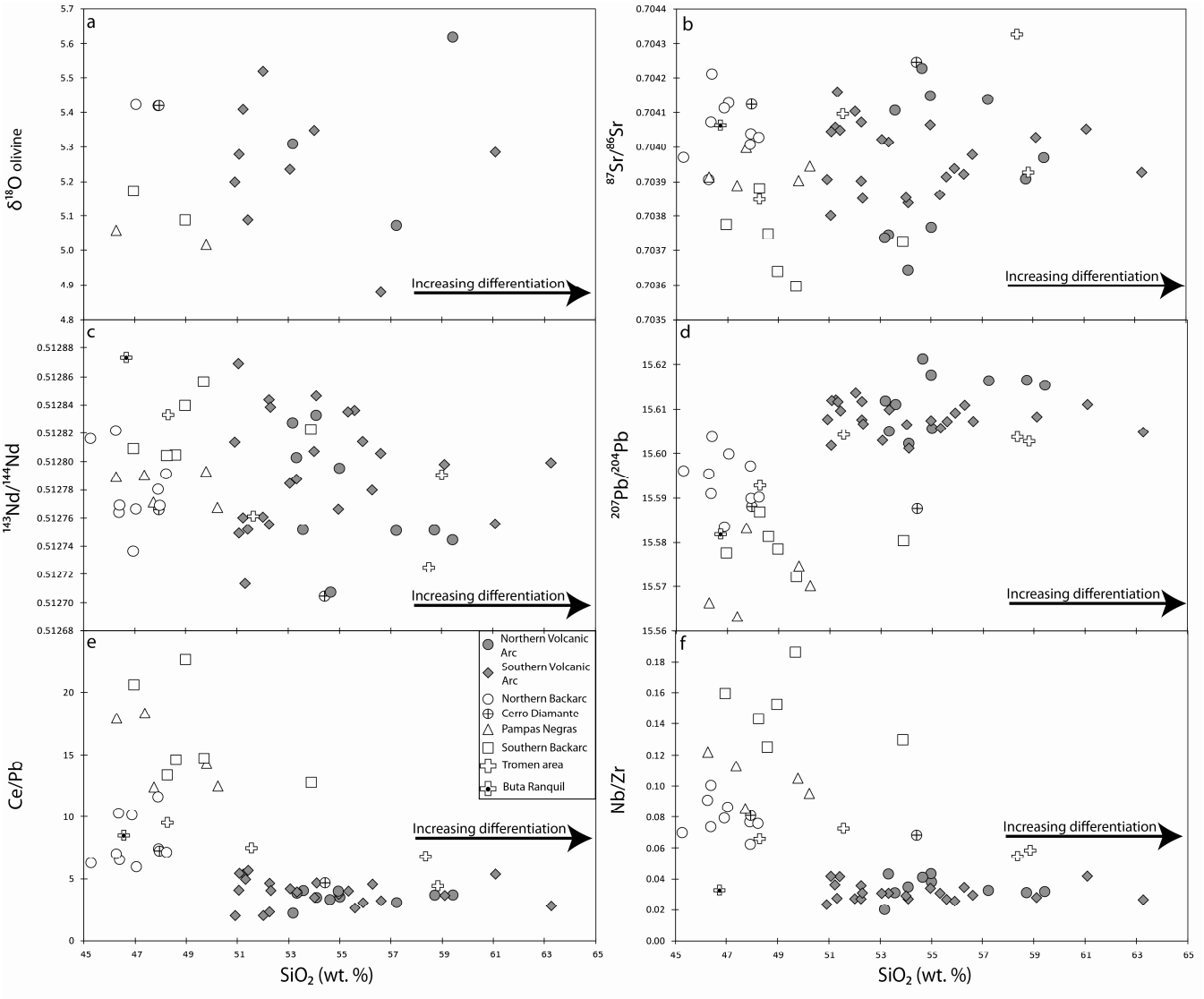

Figure 10

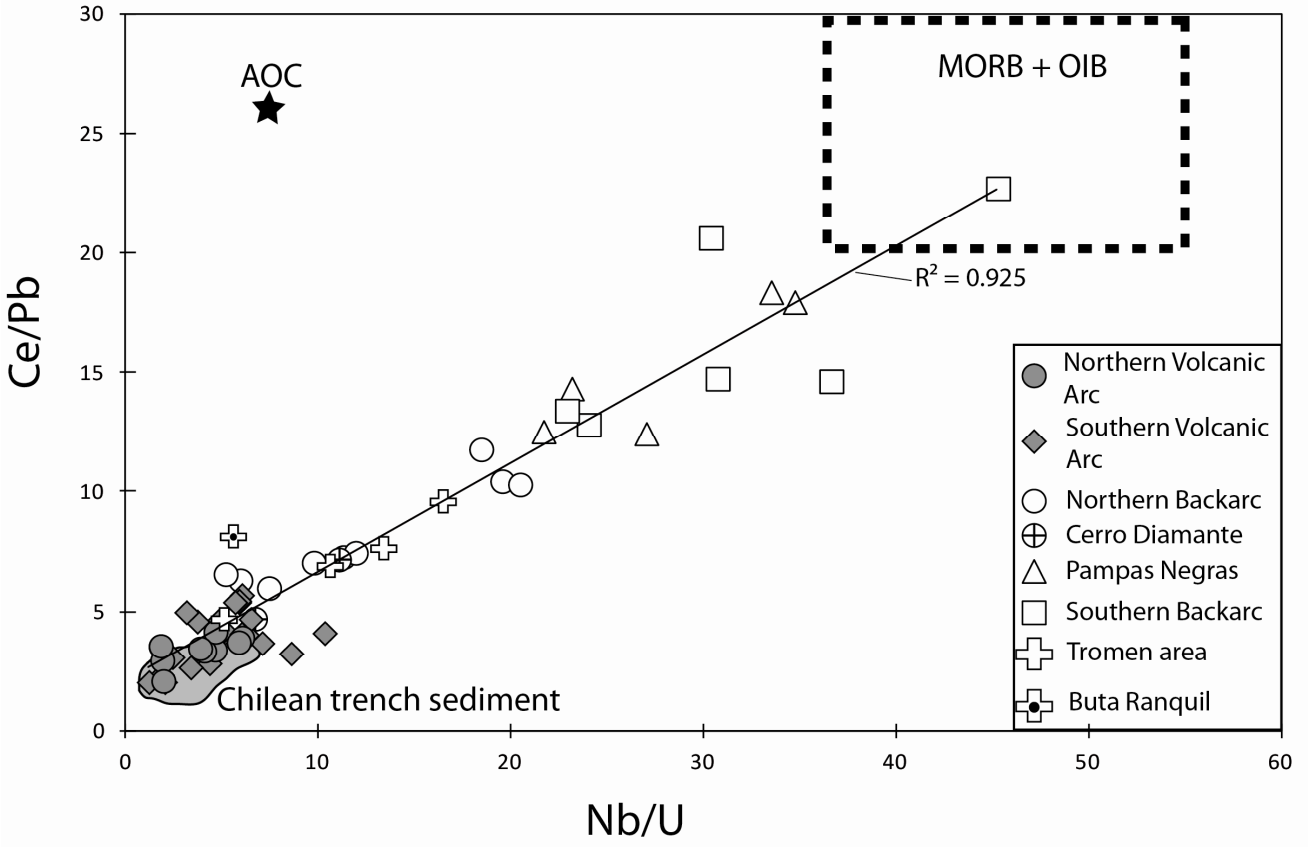

Figure 11

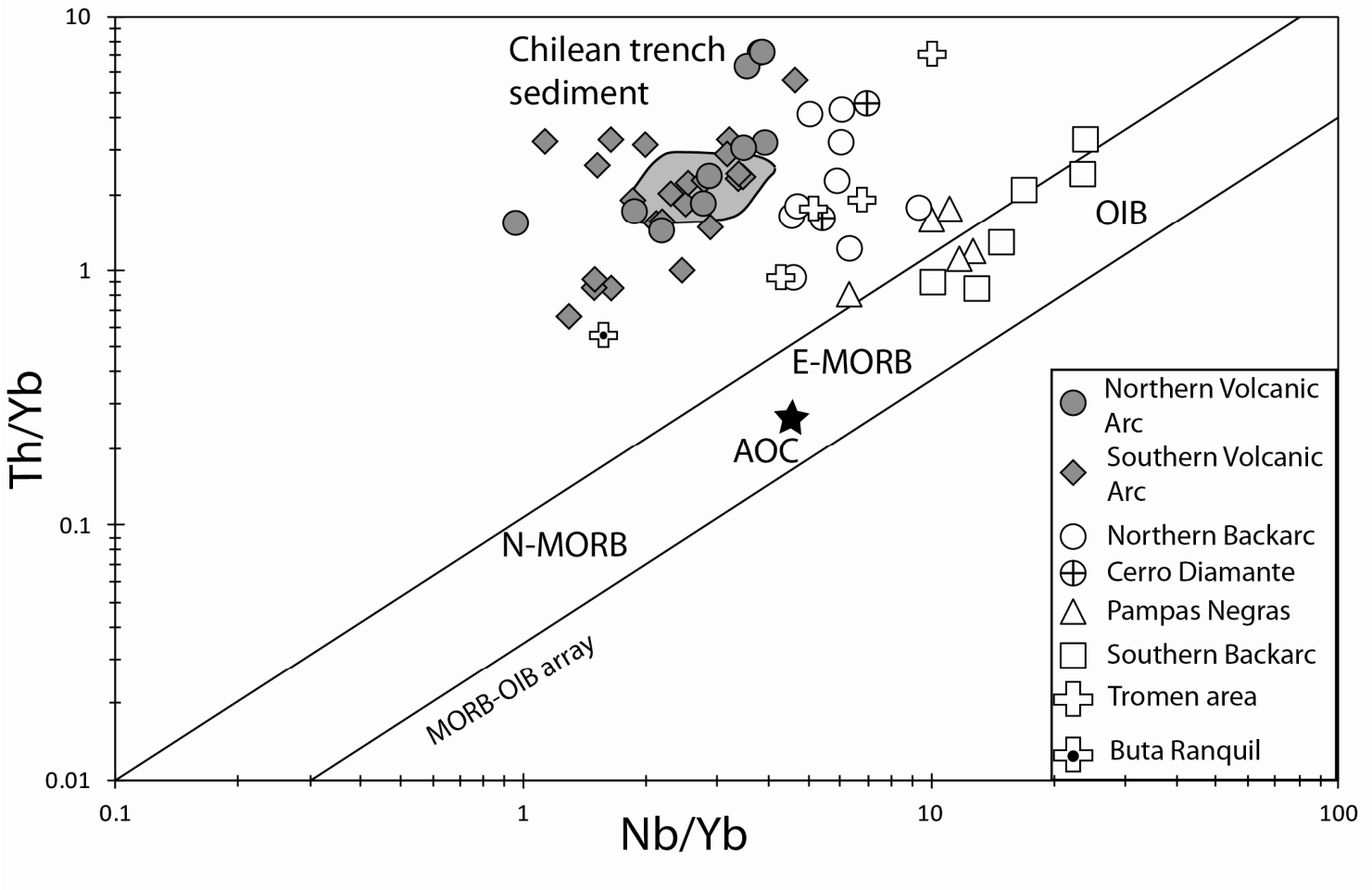

Figure 12

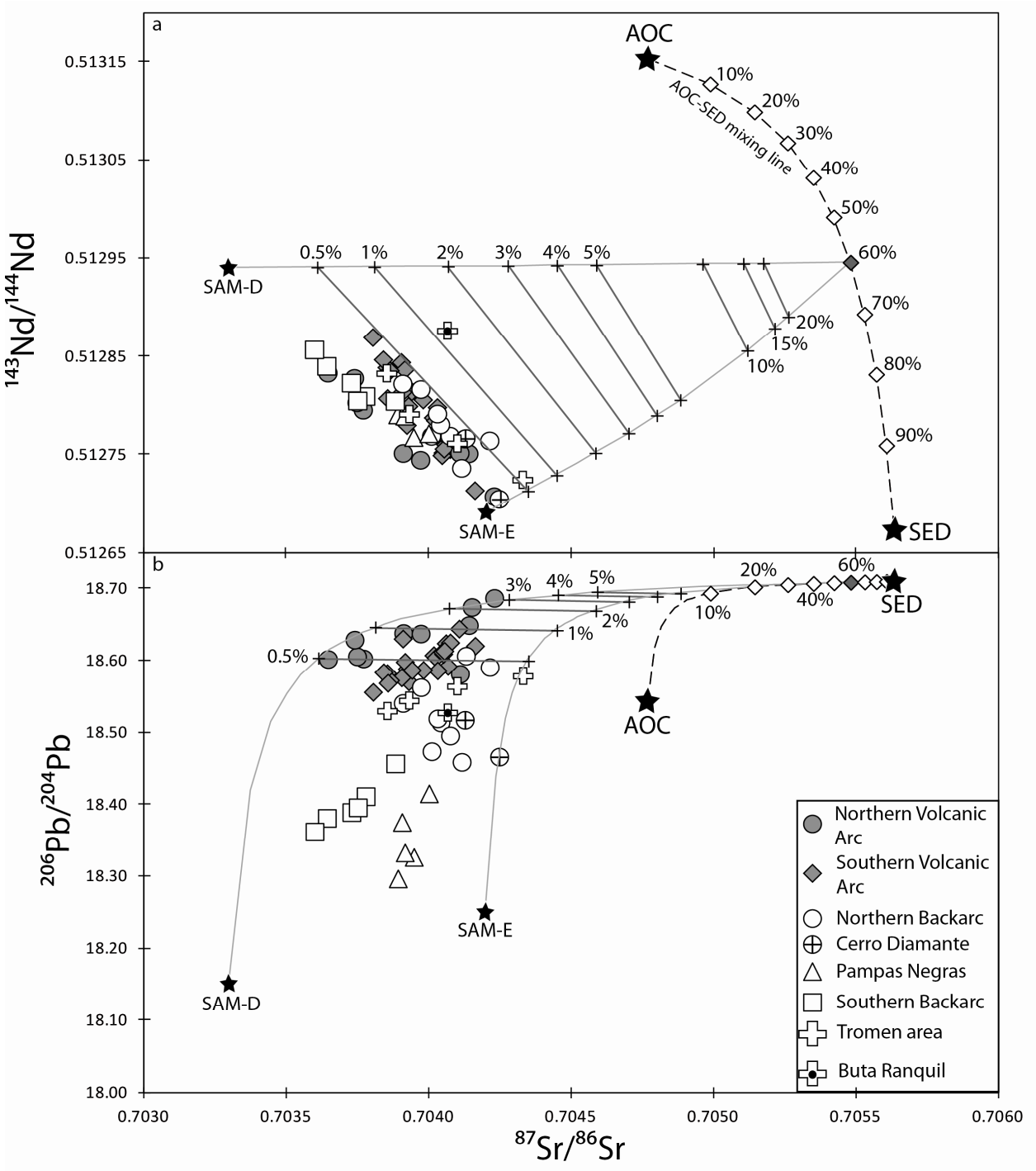

Figure 13